

2010

Higher-Order Physic for Modeling Ice Streams in Ice Sheets

Debra A. Kenneway

Follow this and additional works at: <http://digitalcommons.library.umaine.edu/etd>



Part of the [Fluid Dynamics Commons](#), and the [Glaciology Commons](#)

Recommended Citation

Kenneway, Debra A., "Higher-Order Physic for Modeling Ice Streams in Ice Sheets" (2010). *Electronic Theses and Dissertations*. 265.
<http://digitalcommons.library.umaine.edu/etd/265>

This Open-Access Dissertation is brought to you for free and open access by DigitalCommons@UMaine. It has been accepted for inclusion in Electronic Theses and Dissertations by an authorized administrator of DigitalCommons@UMaine.

HIGHER-ORDER PHYSICS FOR MODELING ICE STREAMS IN ICE SHEETS

By

Debra A. Kenneway

B.A. University of Southern Maine, 2000

M.S. University of Maine, 2005

A THESIS

Submitted in Partial Fulfillment of the

Requirements for the Degree of

Doctor of Philosophy

(in Physics)

The Graduate School

The University of Maine

May, 2010

Advisory Committee:

James L. Fastook, Professor of Computer Science, Advisor

Terence Hughes, Professor of Earth Sciences

Roger LeB. Hooke, Professor of Earth Sciences

Peter O. Koons, Professor of Earth Sciences

Donald P. Mountcastle, Associate Professor of Physics

External Reader:

Jesse V. Johnson, Professor of Computer Science, University of Montana

DISSERTATION
ACCEPTANCE STATEMENT

On behalf of the Graduate Committee for _____, I affirm that this manuscript is the final and accepted thesis. Signatures of all committee members are on file with the Graduate School at the University of Maine, 42 Stodder Hall, Orono Maine.

Committee chair's signature, name, and title

Date:

© 2010 Debra A. Kenneway
All Rights Reserved

LIBRARY RIGHTS STATEMENT

In presenting this thesis in partial fulfillment of the requirements for an advanced degree at The University of Maine, I agree that the Library shall make it freely available for inspection. I further agree that permission for “fair use” copying of this thesis for scholarly purposes may be granted by the Librarian. It is understood that any copying or publication of this thesis for financial gain shall not be allowed without my written permission.

Signature:

Date:

HIGHER-ORDER PHYSICS FOR MODELING ICE STREAMS IN ICE SHEETS

By Debra A. Kenneway

Thesis Advisor: James L. Fastook

An Abstract of the Thesis Presented
in Partial Fulfillment of the Requirements for the
Degree of Doctor of Philosophy
(in Physics)
May, 2010

Ice streams are transitional between inland glaciers and ice shelves. Hence no stresses can be neglected. Ice streams are important dynamic features of a glacier; it is well known that ice streams drain up to 90% of the ice from an ice sheet. Herein I model ice streams as a multiphysics system of coupled components. This includes treating ice as a non-Newtonian fluid since empirical measurements show a power law relation between stress and strain rate. Sliding is a physical feature that must be included. This is done with a novel approach to sliding by way of a slippery layer. The slippery layer is given negligible thickness and rheology is tuned to the ice stream being modeled.

Testing and benchmarking verifies the model. The first comparison is made with the shallow ice approximation, a known analytical solution. The model is setup with a problem domain in which basal stress dominates. Comparison of the surface velocities shows excellent agreement. A second comparison involves a problem domain where longitudinal stress dominates. In this case a floating slab of is tested for

creep via Weertman thinning. The model solution shows excellent agreement with the analytical solution of Weertman thinning.

Additional benchmarking tests other model parameters to ensure proper settings. These include proper discretization of the problem domain and analysis of aspect ratio effects, the ratio of width to height. The temperature solver is tested for conduction dominated problem domains as well as advection and strain heating dominated problem domains. Again the model yields expected results.

The model application to a real world ice stream is made with Whillans Ice Stream, which is located in Antarctica. Model results show that temperature is dominated by advection and that velocities show nearly plug-flow, in which vertical columns of ice move. The slippery layer tuned with a uniform softening shows better agreement with measured surface velocities [17] than tuning with a progressive softening.

ACKNOWLEDGEMENTS

First I would like to thank Jim Fastook for his guidance and support throughout this work. I would like to thank Terry Hughes for support and valuable input. I would like to thank Roger Hooke for all of his careful readings and suggestions in writing this thesis. I would like to thank Peter Koons for his helpful input and insight. I would like to thank Donald Mountcastle for all of his helpful suggestions.

I would like to thank Betty Lee and Pat Byard for all of their helpful assistance with paperwork. I would like to thank Linda Maynard and Leisa Preble for all of their help and assistance over the years.

I would like to thank my family and friends for all of their interest and many wonderful questions.

This work is part of the project Science and Technology Center: Ice Sheets and Sea Level Rise by National Science Foundation/University of Kansas, Grant # FY2005-111C.

TABLE OF CONTENTS

ACKNOWLEDGEMENTS	iii
LIST OF TABLES	vii
LIST OF FIGURES	viii
Chapter	
1 INTRODUCTION	1
2 THE MODEL	4
2.1 The Slippery Layer	4
2.2 Background	5
2.2.1 Stress	5
2.2.2 Tensors	7
2.2.3 Strain Rate	9
2.3 Setting up the Problem	11
2.3.1 Continuity Equation	11
2.3.2 Conservation of Momentum	13
2.3.3 Constitutive Relation	14
2.3.4 The Velocity Differential Equation	15
2.3.5 Stress Boundary Conditions	16
2.4 Incorporating Temperature	17

2.4.1	Advection	17
2.4.2	Conduction	19
2.4.3	Strain Heating	19
2.4.4	Temperature Differential Equation	20
2.4.5	Temperature Boundary Conditions	20
2.4.6	Peclet Number	21
2.5	Summary of Problem Statement	21
2.6	Literature Review	22
3	METHOD	24
3.1	Weak Form	25
3.1.1	Velocity	25
3.1.2	Temperature	27
3.2	Interpolation Functions	28
3.3	Finite Element Model	29
3.3.1	Velocity	30
3.3.2	Temperature	32
3.4	Upwinding	34
3.5	Elements	36
3.6	Integrating	37
3.7	The Solver	38
3.8	Picard Method	38
3.8.1	Velocity Convergence Test	38

3.8.2	Temperature Convergence Test	39
3.8.3	Convergence Acceleration Parameter	39
4	RESULTS	40
4.1	Verification	40
4.1.1	Experiment Setups	40
4.1.2	Rectangular Domain	44
4.1.3	Elliptical Domain	56
4.1.4	Uniform Slab of Floating Ice	60
4.1.5	Thermodynamic Studies	62
4.2	Whillans Ice Stream	70
5	CONCLUSIONS	81
	BIBLIOGRAPHY	83
	BIOGRAPHY OF THE AUTHOR	86

LIST OF TABLES

Table 4.1	Experiment A setup.	41
Table 4.2	Experiment B setup.	42
Table 4.3	Experiment C setup.	43
Table 4.4	List of mesh resolution metrics tested.	45
Table 4.5	List of aspect ratios tested.	48
Table 4.6	List of convergence acceleration parameters and the number of steps taken to converge.	54
Table 4.7	List of values used to calculate the surface velocity of an ice sheet with an elliptical profile.	57
Table 4.8	Results from model runs for comparison of surface velocity with the shallow ice approximation.	58
Table 4.9	List of values used to calculate the Weertman thinning rate of a uniform slab of ice.	61

LIST OF FIGURES

Figure 4.1	Testing the number of elements, domain with nodes.	46
Figure 4.2	Testing the mesh resolution.	47
Figure 4.3	Testing the aspect ratio, domain with nodes.	49
Figure 4.4	Testing the aspect ratio.	50
Figure 4.5	Testing the aspect ratio.	52
Figure 4.6	Testing the tolerance level.	53
Figure 4.7	Testing the tolerance level.	55
Figure 4.8	Elliptical domain, velocity field.	59
Figure 4.9	Uniform slab, strain rate.	61
Figure 4.10	Second run for comparison with Weertman thinning.	64
Figure 4.11	Thermodynamic test with a steady-state slab of ice, isother- mal boundaries.	65
Figure 4.12	Thermodynamic test with a steady-state slab of ice, con- duction.	66
Figure 4.13	Advection thermodynamic test.	68
Figure 4.14	Advection thermodynamic test, temperature profile.	69
Figure 4.15	Plot of node configuration for Whillans Ice Stream with the basal slippery layer.	71

Figure 4.16	Plot of aspect ratio for Whillans Ice Stream with the basal slippery layer.	72
Figure 4.17	Plot of x -component of velocity for Whillans Ice Stream.	73
Figure 4.18	Profile plot of x -component of velocity for Whillans Ice Stream.	73
Figure 4.19	Plot of y -component of velocity for Whillans Ice Stream.	74
Figure 4.20	Plot of velocity magnitude for Whillans Ice Stream.	75
Figure 4.21	Plot of horizontal strain rate for Whillans Ice Stream.	75
Figure 4.22	Plot of vertical strain rate for Whillans Ice Stream.	76
Figure 4.23	Plot of the ice hardness for Whillans Ice Stream with the basal slippery layer.	76
Figure 4.24	Plot of velocity magnitude for Whillans Ice Stream, com- parison of softening in the basal slippery layer.	77
Figure 4.25	Plot of surface velocity for Whillans Ice Stream with the basal slippery layer.	78
Figure 4.26	Plot of surface velocity for Whillans Ice Stream with the basal slippery layer softening comparison.	78
Figure 4.27	Plot of peclet number for Whillans Ice Stream.	79
Figure 4.28	Plot of thermal effects of strain heating for Whillans Ice Stream.	80
Figure 4.29	Plot of temperature for Whillans Ice Stream.	80

Chapter 1

INTRODUCTION

Glaciers undergo sheet flow, stream flow, and shelf flow. Both sheet flow and shelf flow have been well studied and modeled. Sheet flow is often modeled using the shallow-ice approximation. This approach neglects all stresses except the basal drag. The assumption is good for inland ice but may be poor for fast-flowing ice streams with low-surface slope, where longitudinal stresses may not only be important, but also on occasion dominant [12]. Shelf flow is modeled using the Morland equations [32]. A main assumption in deriving the Morland equations is that there is no basal drag, a shear stress, because the ice is supported by water. So with shelf flow it is the longitudinal tension that is balanced against gravitational forcing. Stream flow is transitional between sheet flow and shelf flow. Hence for stream flow both basal shear stresses and longitudinal stresses are important.

A higher-order approach is to couple the mass- and momentum-conservation equations (the prognostic and diagnostic equations [28]) and solve them with no neglected stresses. In this work I develop a finite element computer model for a full-momentum solver in two dimensions to be embedded in the map-plane University of Maine Ice Sheet Model (UMISM) [11]. The two-dimensional simplification models a vertical slice through the ice sheet along a flowline. The two-dimensional model allows us to do two things: 1) implement and test the complex boundary conditions that must be specified for a full-momentum three-dimensional solver, and 2) evaluate when and where longitudinal stresses are important or even dominant.

The differential equation describing conservation of momentum (also referred to as the “balance of forces”) may be solved with either Dirichlet or Neumann boundary conditions [22]. In the Dirichlet condition, the velocity is specified. In the Neumann

condition, the force applied on the boundary is specified. Where the bed is frozen, Dirichlet boundary conditions are the obvious choice, as the velocity is zero and can be specified as such. Where the bed is not frozen, and sliding is occurring (for example, in ice streams, where the shallow-ice approximation breaks down), velocity cannot be specified, but instead the force exerted on the ice by the bed in resisting its forward motion must be specified. The basal drag cannot exceed the driving stress and if it equals the driving stress, then the shallow-ice solution results. A temptation is to use some fraction of the driving stress, and indeed, this approach does produce the concave profile characteristic of an ice stream, but the fraction is hard to define (a model parameter). A better approach is to use a slippery layer which allows: 1) Dirichlet-type specification of zero velocity on the boundary and 2) greater deformation within the slippery layer to simulate sliding at the bed. The soft layer can be interpreted either as a deformable till (deformable subglacial sediments [39]) or as a layer of water-saturated ice at the melting point. In either case its thickness will be negligible compared with the ice thickness, and while the geometry and mechanical properties (how thick and how soft) are still difficult to define, at least they have a physical meaning, which is a good thing for a model parameter to have.

The study of stream flow is relatively new, starting about 30 years ago [23]. Stream flow is important to understanding glaciers and the response of glaciers to climate change. In Antarctica it is well known that stream flow drains up to 90% of the ice from the ice sheet while occupying only 10% of the volume. It has also been proposed that stream flow could play a role in the collapses of the West Antarctic Ice Sheet [1], the collapse of which could cause sea level to rise by as much as 3.3 m [3].

This thesis is organized as follows. Chapter 2 provides background information. The slippery layer approach is described. Next mathematical quantities such as

stress and strain rate are discussed. The problem is set up with derivations of all equations including the incorporation of temperature. The chapter ends with a literature review.

The finite element method as applied to this study is described in Chapter 3. The fundamental components of the method discussed include the weak form, interpolation functions, the finite element model, elements, integrating, and solving. Derivations of the weak form and finite element models are given. A description of upwinding (also called artificial diffusion, a numerical modification that helps with numerical problems that arise when advection dominates the flow of heat) is given.

In Chapter 4 I present my results. This includes presentation of verification studies which include sensitivity studies, comparison with known approximations, and thermodynamic studies. The chapter concludes with presentation of results for the Whillans Ice Stream.

In Chapter 5 I give my conclusions and suggestions for future work related to this study.

Chapter 2

THE MODEL

The model consists of a chunk of glacier ice with known surface and bed profiles. The two-dimensional version consists of a flowline and the three-dimensional version consists of a volume of ice. Both cases incorporate a slippery layer. The following assumptions are made: firn thickness is negligible compared to ice thickness (firn is snow that has fallen on the ice and has survived at least one year [19]); Ice is assumed to be both isotropic and incompressible. This chapter includes discussion of the slippery layer as well as background material. The mathematical description of the model is given by coupled velocity and temperature differential equations. Derivations, using first principles, of the differential equations are given. The chapter concludes with a literature review.

2.1 The Slippery Layer

The slippery layer is a model parameter introduced to help with specifying the boundary conditions at the bed. It has three degrees of freedom, namely how much of the profile in which it is defined, how thick it is, and how soft it is. The slippery layer is a thin layer between the ice and the bed, and runs a specified percentage of the length of the modeled flowline. The glacier is made slightly thicker by dropping the slippery layer into the bed. It is specified with negligible thickness compared to the thickness of the ice. The slippery layer is defined using the material properties of ice but is given a softer rheology than the ice above it. Allowing greater deformation in this layer simulates sliding ice while preserving Dirichlet type specification of zero velocity on the boundary at the bed. The slippery layer can be interpreted as deformable till or water-saturated ice at the melting point.

2.2 Background

This following gives a brief introduction to mathematical quantities needed to model ice streams. Quantities introduced include stress, key features of tensors, and strain. Sign conventions and notation are also included.

2.2.1 Stress

Stress is force per area applied to a surface and has units of Newtons per meter squared (N m^{-2}). A shear stress results from a force applied parallel to the surface, while a normal stress results from force acting perpendicular to the surface. Normal stresses are either compressive or tensile. A force applied to the surface at some angle other than 90° results in both shear and normal stresses on the surface.

Stress is a second rank tensor and is denoted by σ_{ij} where $i, j = x, y$, or z . The first subscript denotes the direction of stress, and the second subscript denotes the direction of the normal to the surface on which the stress is acting. Writing terms this way makes it easy to write equations in matrix notation where i is the row and j is the column, (i.e. all i -components are in the same row). Notation for terms with two subscripts is not standard, and some authors reverse the order so j is the direction and i is the normal. If $i \neq j$ the stress is a shear stress and if $i = j$ it is a normal stress. Some authors use τ for shear stresses and σ only for normal stresses (e.g. σ_{ii}).

The sign convention for positive normal stress components is as follows. A stress component is positive when both the force i and normal j point in the same direction. For example, σ_{xx} is positive when both the normal and the force are in the positive x -direction; the stress component points in the direction of the force. Hence, tension is positive and compression is negative. There is also a sign convention for positive

shear stress components. Shear stress is positive if it would produce counterclockwise rotation.

Another important fact is that the stresses are symmetric. This prevents free rotation during uniform motion. Thus, $\sigma_{ij} = \sigma_{ji}$. Symmetry of stresses reduces the problem of finding nine stresses to that of finding only six.

The problem can be reduced further. Consider a point in a medium. A coordinate system can be defined so that the shear stresses vanish leaving only the three nonzero normal stresses [19]. The normal stresses σ_{ii} are now called principal stresses σ , the coordinate axes are called principal axes, and the normal stresses act on principal planes [14, 19]. The mean normal stress, also called mechanical pressure, is the average of the three principal stresses [31, 36]. The mechanical pressure is written as [31, 36]

$$\bar{p} = -\frac{1}{3}\sigma_{ii} \quad (2.1)$$

or in two dimensions

$$\bar{p} = -\frac{1}{2}\sigma_{ii}.$$

Pressure is hydrostatic when the three principal stresses are equal [31]. Hence hydrostatic pressure is isotropic. Hydrostatic pressure (thermodynamic pressure) and mechanical mean pressure are equal for incompressible materials [31] and ice is approximately incompressible.

Deformation requires non-hydrostatic stress. Total stress can be resolved into two terms:

$$\sigma_{ij} = \sigma'_{ij} - p\delta_{ij} \quad (2.2)$$

where σ'_{ij} , the non-hydrostatic tensor component is called the deviatoric stress (the stress that causes deformation), p is the hydrostatic pressure which is a compressive

stress and therefore subtracted, and δ_{ij} is the Kronecker delta

$$\delta_{ij} = \begin{cases} 1, & \text{if } i = j \\ 0, & \text{if } i \neq j. \end{cases}$$

Note that, owing to the symmetry of the tensor, the deviatoric shear stresses are equal to their total counterparts since $\sigma'_{ij} = \sigma_{ij}$ for $i \neq j$.

2.2.2 Tensors

The variables of interest include stresses, strain rates, position, velocity, and elevations above sea level of the ice surface and bed. These quantities are tensors. The number of “things” needed to specify any one of these quantities, not including magnitude, equals the tensor rank. Scalars, quantities with magnitude only, are tensors of rank zero; vectors, quantities with magnitude and direction such as velocity, are tensors of rank one; and stresses and strain rates, determined by magnitude, direction, and orientation, are tensors of rank two.

The number of components a tensor has is equal to the problem dimension raised to the tensor rank. For example, in two dimensions, the second rank stress tensor has four ($2^2 = 4$) components, and the velocity tensor has two ($2^1 = 2$) components.

Tensors have quantities called invariants, which do not change with rotation of coordinates. A second rank tensor has three invariants called the first, second, and third invariants. For example, finding the principal stresses also yields the tensor invariants of the second rank stress tensor. Proceed as follows. Consider a stress applied to a surface with normal n . Choose an arbitrary coordinate system at the point of applied stress on the surface. Choose a second coordinate system to be the principal axes by rotating the arbitrary coordinate system until the shear stresses vanish. Balancing the stresses in the x, y, and z directions poses the following eigenvalue problem

$$(\sigma_{ij} - \sigma \delta_{ij})l_i = 0$$

where l_i are the direction cosines. Solving the characteristic equation solves the eigenvalue problem. The characteristic equation is

$$\det(\sigma_{ij} - \sigma \delta_{ij}) = 0$$

Writing out the determinant and arranging terms gives

$$\begin{aligned} & - \sigma^3 + (\sigma_{xx} + \sigma_{yy} + \sigma_{zz})\sigma^2 \\ & - (\sigma_{xx}\sigma_{yy} + \sigma_{xx}\sigma_{zz} + \sigma_{yy}\sigma_{zz} - \sigma_{xy}\sigma_{yx} - \sigma_{xz}\sigma_{zx} - \sigma_{yz}\sigma_{zy})\sigma \\ & + (\sigma_{xx}\sigma_{yy}\sigma_{zz} + \sigma_{xy}\sigma_{yz}\sigma_{zx} + \sigma_{xz}\sigma_{yx}\sigma_{zy} - \sigma_{xx}\sigma_{yz}\sigma_{zy} - \sigma_{xy}\sigma_{yx}\sigma_{zz} - \sigma_{xz}\sigma_{yy}\sigma_{zx}) = 0 \end{aligned} \quad (2.3)$$

Rewrite this using Einstein summation notation as

$$-\sigma^3 + (\sigma_{ii})\sigma^2 - \left(\frac{1}{2}(\sigma_{ii}\sigma_{jj} - \sigma_{ij}\sigma_{ji})\right)\sigma + (\varepsilon_{ijk}\sigma_{i1}\sigma_{j2}\sigma_{k3}) = 0 \quad (2.4)$$

where the roots of σ are the principal axes and ε_{ijk} is the Levi-Civita symbol defined by [26]

$$\varepsilon_{ijk} = \begin{cases} +1, & \text{if the indices are an even permutation of 1, 2, 3} \\ 0, & \text{if an index is repeated} \\ -1, & \text{if the indices are an uneven permutation of 1, 2, 3} \end{cases}$$

In Einstein summation notation, terms with repeated indices are summed over all possible values, such as $i, j = x, y, z$ and terms with commas are differentiated, so $u_{i,j}$ implies $\frac{\partial u_i}{\partial j}$.

Compare equation (2.4) to the following

$$-\sigma^3 + I_1\sigma^2 - I_2\sigma + I_3 = 0 \quad (2.5)$$

where I_i are the invariants. The invariants of a second rank tensor are known to be [26]

$$\begin{aligned} I_1 &= \sigma_{ii} \\ I_2 &= \frac{1}{2}(\sigma_{ii}\sigma_{jj} - \sigma_{ij}\sigma_{ji}) \\ I_3 &= \varepsilon_{ijk}\sigma_{i1}\sigma_{j2}\sigma_{k3} \end{aligned} \quad (2.6)$$

Using equations (2.1) and (2.6) the first invariant, I_1 , of the stress tensor is

$$I_1 = \sigma_{ii} = -np$$

where p is the pressure in n dimensions. Note the negative sign since pressure is compressive. The stress deviator invariants are denoted by J_i [14, 19]. Using equation (2.2) the first invariant of the deviator stress tensor is

$$J_1 = \sigma'_{ii} = 0.$$

The second invariant of the deviator stress tensor, J_2 , is

$$J_2 = \frac{1}{2} (\sigma'_{ii}\sigma'_{jj} - \sigma'_{ij}\sigma'_{ji})$$

Substituting $J_1 = \sigma'_{ii} = 0$

$$-J_2 = \frac{1}{2} \sigma'_{ij}\sigma'_{ji}$$

and the effective stress is

$$(\sigma_e)^2 = -J_2 = \frac{1}{2} \sigma'_{ij}\sigma'_{ji} \quad (2.7)$$

It is the effective stress that is responsible for the deformation of the object [31]. From Odqvist [35], the effective stress was introduced by von Mises as a scalar function of the stress deviator tensor.

2.2.3 Strain Rate

For rigid bodies there are different kinds of strain, ε , depending on the kind of stress, σ , responsible for the deformation. Axial strain results from tensional or compressional stresses, and shear strain results from shear stresses. In general, strain is the change in spatial dimensions of a body divided by the original dimensions. or a relative change. Hence the strain in a wire subject to a tensile stress is the change in length of the wire divided by its original length.

On the other hand, stress is related to strain rate for fluids. This is necessary because in fluids, stress causes immense strain [31]. Ice in the problem domain is treated as a nonlinear fluid [39]. Hence strain rates will be of interest. By definition, the strain rate tensor, $\dot{\varepsilon}_{ij}$, [14, 19] is

$$\dot{\varepsilon}_{ij} = \frac{d\varepsilon_{ij}}{dt} = \frac{1}{2} \left\{ \frac{\partial u_i}{\partial j} + \frac{\partial u_j}{\partial i} \right\} \quad (2.8)$$

where the velocities, u_i and u_j are in the i and j directions with $i, j = x$ or y in two dimensions and $i, j = x, y$, or z in three dimensions. This can also be written as

$$\dot{\varepsilon} = \frac{1}{2} \left\{ \nabla \vec{u} + \{\nabla \vec{u}\}^T \right\} \quad (2.9)$$

where $\nabla \vec{u}$ is the velocity gradient tensor and $\{\nabla \vec{u}\}^T$ is its transpose. The strain rate is the symmetric part of the velocity gradient tensor which has two common representations. For example, many texts on fluid dynamics (e.g. [5, 30, 14, 10]) define $\{\nabla \vec{u}\}_{ij}$ as $u_{i,j}$ and many continuum mechanics texts (e.g. [16, 37]) define $\{\nabla \vec{u}\}_{ij}$ as $u_{j,i}$. Note that the symmetric part of either definition of the velocity gradient yields the same strain rate tensor.

Equation (2.8) written using Einstein summation notation is

$$\dot{\varepsilon}_{ij} = \frac{1}{2} \{u_{i,j} + u_{j,i}\} \quad (2.10)$$

The first two invariants of the strain rate tensor are

$$I_1 = \dot{\varepsilon}_{xx} + \dot{\varepsilon}_{yy} + \dot{\varepsilon}_{zz} = 0 \quad (2.11)$$

and

$$-I_2 = \dot{\varepsilon}_e^2 = \frac{1}{2} (\dot{\varepsilon}_{ij} \dot{\varepsilon}_{ji}). \quad (2.12)$$

Equation (2.12) is also called the effective strain rate. From Odqvist [35] the effective strain rate is found in a manner similar to effective stress.

2.3 Setting up the Problem

The variables we wish to solve for include ice thickness, ice velocity, the various stress and strain rate components, and temperature. In the finite element method, these quantities are evaluated at selected points in the domain. Hence the perspective is the Eulerian as opposed to the Lagrangian description. In the latter the material is fixed and the coordinate system moves. Combining a conservation law with a constitutive relation results in a differential equation. For example, conservation of momentum and the constitutive equation for ice, which relates velocity to stress, yields a differential equation in velocity. Conservation of mass, conservation of momentum, and the constitutive relation are discussed in the following.

2.3.1 Continuity Equation

The continuity equation, a statement of conservation of mass, is found by considering a small cube of ice with volume $dx\,dy\,dz$, mass m , and density ρ . The mass of material moving in the positive x direction with velocity u_x into a side of the cube normal to the x -axis is $\rho u_x\,dy\,dz$, and the mass flowing out the opposite cube side is $\rho u_x\,dy\,dz + \frac{\partial(\rho u_x)}{\partial x} dx\,dy\,dz$. Similar expressions can be written for the other sides. The change in mass with time is expressed as

$$\begin{aligned} \frac{\partial m}{\partial t} = & \rho u_x\,dy\,dz - \left(\rho u_x\,dy\,dz + \frac{\partial(\rho u_x)}{\partial x} dx\,dy\,dz \right) \\ & + \rho u_y\,dx\,dz - \left(\rho u_y\,dx\,dz + \frac{\partial(\rho u_y)}{\partial y} dx\,dy\,dz \right) \\ & + \rho u_z\,dx\,dy - \left(\rho u_z\,dx\,dy + \frac{\partial(\rho u_z)}{\partial z} dx\,dy\,dz \right) \end{aligned}$$

or simplifying

$$\frac{\partial m}{\partial t} = - \left(\frac{\partial(\rho u_x)}{\partial x} + \frac{\partial(\rho u_y)}{\partial y} + \frac{\partial(\rho u_z)}{\partial z} \right) dx\,dy\,dz$$

Because the mass, m , divided by the volume, $dx dy dz$, is the density, this may be rewritten

$$\frac{\partial \rho}{\partial t} + \nabla \cdot [\rho \vec{u}] = 0 \quad (2.13)$$

where $\vec{u} = u_x \hat{i} + u_y \hat{j} + u_z \hat{k}$ is the velocity in Cartesian coordinates. Note this can also be written as

$$\rho_{,t} + [\rho u_i]_{,i} = 0$$

where $\rho_{,t} = \frac{\partial \rho}{\partial t}$. The repeated index i implies summation and the comma means to differentiate with respect to index i .

If the density is constant, implying that the material is incompressible, this becomes

$$\nabla \cdot \vec{u} = 0 \quad (2.14)$$

which can be written as

$$u_{i,i} = 0$$

and we have recovered equation (2.11).

The principle of conservation of mass can be used to write an equation for the variation in thickness of an ice mass over time. Consider a vertical column of ice moving with average horizontal velocity \bar{u} . Denote the mass flux by $q = \bar{u}h$ where \bar{u} is the depth-averaged velocity of the column of ice and h is the thickness. Then the variation in thickness over time t is

$$\frac{\partial h}{\partial t} = \dot{a} - \frac{\partial q_x}{\partial x} - \frac{\partial q_y}{\partial y}$$

and in two dimensions

$$\frac{\partial h}{\partial t} = \dot{a} - \frac{\partial q_x}{\partial x}$$

where q_i is the x or y component of the mass flux and \dot{a} is the surface accumulation rate, which is the ice-equivalent of snowfall with units of meters per year (m a^{-1}).

2.3.2 Conservation of Momentum

Linear momentum is conserved when the sum of forces on an object vanishes [13]. To see this, write Newton's second law as

$$\vec{F} = \frac{d\vec{p}}{dt}$$

where \vec{F} is the sum of forces on an object, $\vec{p} = m\vec{u}$ is the linear momentum of a mass m moving with velocity \vec{u} , and t is time.

Consider a cube of ice with volume $dx dy dz$, mass m , and density ρ . The sum of forces in the x -direction is [19]

$$\begin{aligned} \Sigma F_x = & - \sigma_{xx} dy dz + \left\{ \sigma_{xx} + \frac{\partial \sigma_{xx}}{\partial x} dx \right\} dy dz \\ & - \sigma_{xy} dx dz + \left\{ \sigma_{xy} + \frac{\partial \sigma_{xy}}{\partial y} dy \right\} dx dz \\ & - \sigma_{xz} dx dy + \left\{ \sigma_{xz} + \frac{\partial \sigma_{xz}}{\partial z} dz \right\} dx dy \\ & - \rho g_x dx dy dz \end{aligned}$$

where ρg_x is x -component of the gravitational force on the body. Simplify to find

$$\Sigma F_x = \left[\frac{\partial \sigma_{xx}}{\partial x} + \frac{\partial \sigma_{xy}}{\partial y} + \frac{\partial \sigma_{xz}}{\partial z} - \rho g_x \right] dx dy dz \quad (2.15)$$

By definition

$$\frac{d\vec{p}}{dt} = \frac{d[\rho \vec{u}]}{dt} dx dy dz. \quad (2.16)$$

and the material derivative, also known as the substantial or total or Lagrangian derivative [31, 36] is defined as

$$\frac{D\vec{p}}{Dt} = \frac{\partial \vec{p}}{\partial t} + \vec{u} \cdot \nabla \vec{p} \quad (2.17)$$

Assuming incompressibility, in the x -direction, equate the right hand side of equation (2.16) with the right hand side of equation (2.17) to find

$$\rho \frac{du_x}{dt} dx dy dz = \rho \left[\frac{\partial u_x}{\partial t} + u_x \frac{\partial u_x}{\partial x} + u_y \frac{\partial u_x}{\partial y} \right] dx dy dz \quad (2.18)$$

Hence equating the right hand side of equation (2.18) with the right hand side of equation (2.15) we have

$$\rho \left[\frac{\partial u_x}{\partial t} + u_x \frac{\partial u_x}{\partial x} + u_y \frac{\partial u_x}{\partial y} \right] = \frac{\partial \sigma_{xx}}{\partial x} + \frac{\partial \sigma_{xy}}{\partial y} + \frac{\partial \sigma_{xz}}{\partial z} - \rho g_x$$

Or in summation notation, noting similar equations for the y -, and z -directions

$$\rho [u_{i,t} + u_j u_{i,j}] = \sigma_{ij,j} - \rho g_i \quad (2.19)$$

Note the repeated index j : hence summation is implied and the comma means to differentiate with respect to the second index either j or t for time as specified. Index i can take on three different values so equation (2.19) represents three separate equations.

If the cube is not accelerating (or decelerating), $\Sigma F_x = 0$, so

$$\sigma_{ij,j} - \rho g_i = 0 \quad (2.20)$$

that is the inertial terms, left hand side of equation (2.19), are negligible. Note that the divergence of the stress is equal to the force per volume.

2.3.3 Constitutive Relation

A constitutive relation describes a material property [39]. The Glen flow law for glaciers is a constitutive relation relating stress and strain rate. Derived from fitting experimental data for strain rate versus stress, the Glen flow law [15, 19] is

$$\dot{\epsilon}_e = \left\{ \frac{\sigma_e}{B} \right\}^n \quad (2.21)$$

where B , the ice harness parameter, is a measure of the ice viscosity and depends on temperature. A wide variety of experimental data suggests that $n = 3$ is a good approximation for ice [18]. At its core, equation (2.21) is empirical although there are some physical processes suggestive of such a flow law.

To linearize the problem, let's assume ice is incompressible by assuming that the snow and firn thicknesses are negligible compared to the ice thickness. Let's also assume that ice is isotropic. This simplifying assumption is probably not as good as the previous one of incompressibility since ice has a hexagonal structure, but this will be taken into consideration later. The assumptions of incompressibility and isotropy result in coaxial principal axes of stress and strain rate leading to the following form of the Glen flow law

$$\dot{\epsilon}_{ij} = \frac{\sigma_e^{n-1}}{B^n} \sigma'_{ij} \quad (2.22)$$

where $\dot{\epsilon}_{ij}$ is the strain rate tensor, σ_e is the effective stress, B is a measure of viscosity with units (bars $a^{-1/n}$) where a is annum, and σ'_{ij} is the viscous or deviatoric stress tensor.

Now solve equation (2.21) for σ_e and substitute into equation (2.22) to get

$$\dot{\epsilon}_{ij} = \frac{(\dot{\epsilon}_e)^{\frac{n-1}{n}}}{B} \sigma'_{ij} \quad (2.23)$$

and solving for σ'_{ij}

$$\sigma'_{ij} = (B(\dot{\epsilon}_e)^{\frac{1-n}{n}}) \dot{\epsilon}_{ij}. \quad (2.24)$$

It is important to note that the linearization term, $(B(\dot{\epsilon}_e)^{\frac{1-n}{n}})$, is a mathematical construct needed to solve the problem. Hence the linearization term does not give a useful physical interpretation of data because it is a function of the strain rate.

2.3.4 The Velocity Differential Equation

Start with the equation for total stress, equation (2.2), repeated here for convenience

$$\sigma_{ij} = \sigma'_{ij} - p\delta_{ij}$$

noting it can also be written as

$$\sigma = \sigma' - pI$$

where I is the identity tensor, with value 1 on the diagonal and value 0 everywhere else.

Next substitute for the viscous or deviatoric stress using equation (2.24)

$$\sigma = (B(\dot{\epsilon}_e)^{\frac{1-n}{n}})\dot{\epsilon} - pI$$

Substitute for the strain rate tensor using equation (2.9)

$$\sigma = (B(\dot{\epsilon}_e)^{\frac{1-n}{n}})\frac{1}{2}\left\{\nabla\vec{u} + \{\nabla\vec{u}\}^T\right\} - pI$$

Let $\eta = \frac{1}{2}B(\dot{\epsilon}_e)^{\frac{1-n}{n}}$

$$\sigma = \eta\left\{\nabla\vec{u} + \{\nabla\vec{u}\}^T\right\} - pI$$

Substitute into equation (2.19), which is exact

$$\rho\frac{\partial\vec{u}}{\partial t} + \rho(\vec{u} \cdot \nabla)\vec{u} = \nabla \cdot \left\{\eta\left\{\nabla\vec{u} + \{\nabla\vec{u}\}^T\right\} - pI\right\} - \rho\vec{g} \quad (2.25)$$

Equations (2.14) and (2.25) are called the incompressible Navier-Stokes equations, written in the stress-divergence form.

For non-accelerating systems, $\rho\frac{\partial\vec{u}}{\partial t} + (\vec{u} \cdot \nabla)\vec{u} = 0$. Hence equation (2.25) simplifies to

$$\nabla \cdot \left\{\eta\left\{\nabla\vec{u} + \{\nabla\vec{u}\}^T\right\} - pI\right\} = \rho\vec{g} \quad (2.26)$$

2.3.5 Stress Boundary Conditions

The velocity differential equation resulting from conservation of momentum and Glen's law permit two types of boundary conditions [22]. The first type is Dirichlet in which velocity is specified. Dirichlet boundary conditions can occur at the base

of the ice along the flowline. The second type is Neumann; in this case the force on the boundary is specified. Multiplying stress by area on a boundary specifies force. Typically at the two ends of the flowline, the boundary condition is taken to be a linear variation of the pressure with depth.

2.4 Incorporating Temperature

The temperature distribution in a glacier is affected by advection, conduction, internal heat production, and the temperatures along the boundaries (or boundary conditions). Advection is temperature change due to movement of an element of ice of one temperature into a region in which the equilibrium temperature is different. For flow in two dimensions there is both vertical and horizontal advection. Conduction is the transport of energy due to a temperature gradient within the ice [2]. Paterson [39] discusses internal heat production. The primary sources of internal heat production that we will take into account include strain heating and heat from friction during sliding. Strain heating occurs wherever ice deforms [19]. Other sources of internal heat production include firn compaction and refreezing of meltwater in the firn; we will neglect both of these. The differential equation describing the temperature distribution is found by conserving energy. Derivations of the various terms follows.

2.4.1 Advection

The internal energy in a volume of ice of size $dx\ dy\ dz$ is $\rho c \Delta T dx dy dz$ where T is the temperature in Kelvins and $c = c(T)$ is the specific heat capacity of the material which depends on temperature. The change in energy due to advection is evaluated by considering flow of ice of temperature T into the volume with velocity $\vec{u} =$

$u_x \hat{i} + u_y \hat{j} + u_z \hat{k}$. In the x -direction, the energy transferred into the volume per unit time is $u_x dy dz \rho c \Delta T$ and that leaving the volume is $u_x dy dz \rho c \left(\Delta T + \frac{\partial T}{\partial x} dx \right)$.

Similar expressions are written for the energy transferred in the y - and z -directions. Thus the change in energy per time, expressed as the change in heat, q , transferred per time, t , in the cube of ice is

$$\begin{aligned} \frac{\partial q}{\partial t} = & u_x dy dz \rho c \Delta T - u_x dy dz \rho c \left(\Delta T + \frac{\partial T}{\partial x} dx \right) \\ & + u_y dx dz \rho c \Delta T - u_y dx dz \rho c \left(\Delta T + \frac{\partial T}{\partial y} dy \right) \\ & + u_z dx dy \rho c \Delta T - u_z dx dy \rho c \left(\Delta T + \frac{\partial T}{\partial z} dz \right) \end{aligned}$$

which simplifies to

$$\frac{\partial q}{\partial t} = -\rho c dx dy dz \left(u_x \frac{\partial T}{\partial x} + u_y \frac{\partial T}{\partial y} + u_z \frac{\partial T}{\partial z} \right).$$

This can be rewritten as

$$\frac{1}{\rho c dx dy dz} \frac{\partial q}{\partial t} = -(\vec{u} \cdot \nabla T).$$

Note that

$$\frac{1}{\rho c dx dy dz} \frac{\partial q}{\partial t} = \frac{\partial T}{\partial t} \quad (2.27)$$

since density ρ has units (kg m^{-3}), specific heat c has units ($\text{J kg}^{-1} \text{K}^{-1}$), $dx dy dz$ has units (m^3), and $\partial q / \partial t$ has units (J a^{-1}) where (a) is time units in years resulting in units of Kelvin per year (K a^{-1}). Hence

$$\frac{\partial T}{\partial t} = \frac{1}{\rho c dx dy dz} \frac{\partial q}{\partial t} = -(\vec{u} \cdot \nabla T). \quad (2.28)$$

The minus sign indicates that when both the temperature gradient and the velocity are positive, the temperature decreases because ice moving into the volume is colder than that leaving it.

2.4.2 Conduction

We find the conduction term as follows. As with advection, we consider a cube of ice with dimensions $dx \, dy \, dz$, density ρ , and specific heat c . The heat flux, H , into one side of the cube in the x -direction is $k \, dy \, dz \, \frac{\partial T}{\partial x}$ where $k = k(T)$ is the thermal conductivity, a function of temperature, with units Joules per meter-year-Kelvin ($\text{J m}^{-1} \text{a}^{-1} \text{K}^{-1}$), $dy \, dz$ is the area of the cube face with units (m^2), and T is the temperature in Kelvin (K). The heat flux out of the cube is $k \, dy \, dz \, \frac{\partial T}{\partial x} + \frac{\partial}{\partial x} \left(k \, dy \, dz \, \frac{\partial T}{\partial x} \right) dx$. Again, similar equations can be written in the y - and z -directions. The change in heat flux is thus

$$\begin{aligned} \frac{\partial q}{\partial t} = & k \, dy \, dz \, \frac{\partial T}{\partial x} + \frac{\partial}{\partial x} \left(k \, dy \, dz \, \frac{\partial T}{\partial x} \right) dx - k \, dy \, dz \, \frac{\partial T}{\partial x} \\ & k \, dx \, dz \, \frac{\partial T}{\partial y} + \frac{\partial}{\partial y} \left(k \, dx \, dz \, \frac{\partial T}{\partial y} \right) dy - k \, dx \, dz \, \frac{\partial T}{\partial y} \\ & k \, dx \, dy \, \frac{\partial T}{\partial z} + \frac{\partial}{\partial z} \left(k \, dx \, dy \, \frac{\partial T}{\partial z} \right) dz - k \, dx \, dy \, \frac{\partial T}{\partial z} \end{aligned}$$

which simplifies to

$$\frac{\partial q}{\partial t} = \frac{\partial}{\partial x} \left(k \, dy \, dz \, \frac{\partial T}{\partial x} \right) dx + \frac{\partial}{\partial y} \left(k \, dx \, dz \, \frac{\partial T}{\partial y} \right) dy + \frac{\partial}{\partial z} \left(k \, dx \, dy \, \frac{\partial T}{\partial z} \right) dz.$$

Since we are dealing with an Eulerian system, dx , dy , and dz are not functions of x, y , or z so this can be rewritten as

$$\frac{1}{dx \, dy \, dz} \frac{\partial q}{\partial t} = \nabla \cdot [k \nabla T]$$

or using equation (2.27)

$$\frac{\partial T}{\partial t} = \frac{1}{\rho c} \nabla \cdot [k \nabla T]. \quad (2.29)$$

2.4.3 Strain Heating

Strain heating occurs when ice deforms. The rate of heat generated due to the deformation is equal to the work done per unit time. This can be shown to be [19]

$$\frac{1}{\rho c \, dx \, dy \, dz} \frac{\partial q}{\partial t} = \frac{\sigma_e \dot{\epsilon}_e}{\rho c}$$

and is usually written as

$$\frac{\partial T}{\partial t} = \frac{Q}{\rho c} \quad (2.30)$$

where Q is strain heating (not to be confused with activation energy Q) and has units of Newtons per meter²-year ($\text{N m}^{-2} \text{ a}^{-1}$), so $\partial T/\partial t$ is in Kelvin per year (K a^{-1}). See Hooke [19] or Paterson [39] for details.

2.4.4 Temperature Differential Equation

We find the change in temperature T with time t by adding the conduction, advection, and strain heating terms, thus

$$\frac{\partial T}{\partial t} = \frac{1}{\rho c} \nabla \cdot [k \nabla T] - \vec{u} \cdot \nabla T + \frac{Q}{\rho c}. \quad (2.31)$$

We can expand equation (2.31) using the vector identity $\nabla \cdot \phi \vec{F} = \phi \nabla \cdot \vec{F} + \vec{F} \cdot \nabla \phi$ where in our case ϕ is $\frac{k}{\rho c} = \kappa$, the thermal diffusivity with units meters squared per year ($\text{m}^2 \text{ a}^{-1}$), and \vec{F} is ∇T , noting that $\nabla \cdot \nabla T = \nabla^2 T$

$$\frac{\partial T}{\partial t} = \kappa \nabla^2 T + \frac{1}{\rho c} \nabla k \cdot \nabla T - \vec{u} \cdot \nabla T + \frac{Q}{\rho c}. \quad (2.32)$$

2.4.5 Temperature Boundary Conditions

As with conservation of momentum, there are two types of boundary conditions, Dirichlet (state variable specified) and Neumann (flux specified) [22]. Note that the differential equation can be solved with either boundary condition. The one chosen depends on what is known about the system. The Dirichlet boundary condition is appropriate for the ice surface where the temperature is taken to be the mean annual air temperature and is estimated from

$$T = T_{base} + \gamma z_e \quad (2.33)$$

where T_0 is an initial temperature in degrees Celsius ($^{\circ}\text{C}$), γ is the atmospheric lapse rate with units degrees Celsius per kilometer ($^{\circ}\text{C km}^{-1}$), the rate of change in

temperature with elevation, and y_e is the elevation in kilometers (km). The lapse rate is negative because temperature decreases as elevation increases. The Neumann boundary condition is appropriate for the bed when the temperature there is below the melting point. The flux involved is the heat coming from within the earth, the geothermal flux. This is specified by

$$\frac{\partial T}{\partial z} = -\frac{G}{k} \quad (2.34)$$

where G is the geothermal flux in Joules per meter squared per year ($\text{J m}^{-2} \text{a}^{-1}$). When the bed is at the melting point a Dirichlet condition is appropriate: the temperature at the bed equals the pressure melting point.

2.4.6 Peclet Number

The Peclet number compares convection in fluids and advection in solids to diffusion. The Peclet number, \vec{P} , will be large if advection dominates diffusion or if diffusion is very small, and it will be small if diffusion dominates advection. It is defined as [25, 38, 6]

$$\vec{P} = \frac{\vec{u} L}{\left(\frac{k}{\rho c_p}\right)}$$

where \vec{u} is the velocity, ρ is the density, c_p is the specific heat, L is a characteristic length, and k is the thermal conductivity. The numerator is a measure of advection while the denominator is a measure of conduction.

2.5 Summary of Problem Statement

The following summarizes the problem for a non-accelerating, isotropic, incompressible, viscous fluid. The incompressibility condition is

$$\nabla \cdot \vec{u} = 0.$$

The velocity equation (2.26) and temperature equation (2.31), repeated here for convenience, are

$$\nabla \cdot \left\{ \eta \left\{ \nabla \vec{u} + \{ \nabla \vec{u} \}^T \right\} - pI \right\} = \rho \vec{g} \quad (2.35)$$

and

$$\frac{\partial T}{\partial t} = \frac{1}{\rho c} \nabla \cdot [k \nabla T] - \vec{u} \cdot \nabla T + \frac{Q}{\rho c}.$$

where \vec{u} is the velocity of the ice, p is the mean normal stress, $\eta = \frac{1}{2}B(T)\dot{\epsilon}_e^{\frac{1-n}{n}}$ is the effective viscosity, n is the flow law power, taken to be 3, ρ is the ice density, g is the acceleration due to gravity, T is the temperature of the ice, k is the thermal conductivity of ice, and c is the specific heat capacity.

Each differential equation requires boundary conditions specified over the entire boundary [41]. Thus, velocity and force must be specified so that they cover the entire boundary without overlapping; that is, the boundary can be divided into pieces and each piece must have either velocity specified or force specified. Similarly temperature and heat flux must be specified so that the entire boundary is covered with no overlapping of the specifications. Note that the equations are coupled since the velocity has temperature dependence in the effective viscosity, and temperature depends on the ice strain rate through Q .

2.6 Literature Review

Robin solved the problem of a stable ice sheet with steady state temperatures and with conduction and vertical advection but no horizontal advection [42]. To simplify the problem, he solved it at the ice divide (highest point), so he could assume negligible horizontal velocities and negligible strain rates. He also assumed that temperatures were symmetric about the divide. Robin found temperatures show error function behavior. See [19] or [39] for more details.

Dahl-Jensen [8] also solved for steady state temperatures in an ice sheet. She uses a coordinate scaling. One of Dahl-Jensen's assumptions requires a nearly horizontal bed (slope = 0). The coordinate scaling also allows her to neglect conduction in the horizontal plane as well as strain heating in the vertical direction. Dahl-Jensen uses a backward finite difference scheme to solve the equations. She calculates results for a horizontal bed. Plots of temperature show an inversion that becomes more pronounced closer to the grounding line; that is the coldest temperatures are in the body of the ice not at the surface.

Budd et al. [7] calculated steady state temperature profiles away from the divide in a model called the Column model. Budd applied strain heating at the bed, incorporating strain heating into the geothermal flux. He also approximated the horizontal advection term with velocity multiplied by temperature varying linearly with depth. Temperature profiles plotted using his solution for data from Greenland also show an inversion because cold ice is advected from the surface upstream. See Hooke [19] for more details.

There are several other modelers who have modeled ice sheets using thermodynamically coupled equations and the shallow ice approximation (e.g. MacAyeal [27] and Huybrechts [24]). Herein, I model ice sheets using thermodynamically coupled equations with full momentum equations, thus avoiding the shallow ice approximation.

Chapter 3

METHOD

The finite element method is used to solve the coupled velocity and temperature differential equations. The problem domain contains an interior, Ω , and a boundary, Γ . First, subdividing the problem domain into elements forms the mesh. The elements cover the problem domain entirely without overlapping. The average size of the elements determines the resolution of the mesh. Next, an approximate solution is found at each element by writing it as a linear combination of polynomials multiplied by constants. The final step is to combine the element solutions.

Restating the problem in a so-called weak form lessens continuity and differentiability conditions and allows irregularities in the data. Deriving the weak form consists of the following steps. First, form the residual by moving all terms to one side of the equation. Next multiply by a weighting function, also called a test function, and integrate element-wise. Integrating by parts makes the problem symmetric in the unknowns and weighting function. The Galerkin method chooses basis functions for the weight functions. Basis functions are orthogonal, linearly independent functions used to represent other functions in a function space. Lagrange functions are basis functions consisting of polynomials.

The finite element approximate solution must satisfy conditions in order to find the correct solution; e.g., continuity requirements as required by the weak form must be satisfied. The polynomials must include all appropriate terms; that is they must be complete, and they must also be linearly independent [41]. The polynomials are interpolation functions, and one choice is Lagrange functions.

The finite element model of the problem then consists of substituting the approximate solution into the weak form and summing over all of the elements. Choose the

weight functions to be Lagrange interpolation functions. Finally, write the resulting equations in matrix form. Determining the coefficient matrices solves the problem.

3.1 Weak Form

This section contains the weak form derivations for velocity and temperature.

3.1.1 Velocity

Start with the velocity equation (2.26) repeated here for convenience

$$\nabla \cdot \left\{ \eta \left\{ \nabla \vec{u} + \{ \nabla \vec{u} \}^T \right\} - pI \right\} = \rho \vec{g}$$

The first step in constructing the weak form is to find the residual error using equation (2.26).

$$\vec{r} = \nabla \cdot \left\{ \eta \left\{ \nabla u + \{ \nabla u \}^T \right\} - pI \right\} - \rho \vec{g}$$

where in two dimensions $\vec{r} = \vec{r}(x, y)$ and in three dimensions $\vec{r} = \vec{r}(x, y, z)$. The following is the derivation in three dimensions.

To do this we multiply by a test function $\vec{v} = \vec{v}(x, y, z)$ and integrate over the domain Ω of the problem (i.e. volume V)

$$\int_{\Omega} \vec{v} \cdot \vec{r} dV = \int_{\Omega} \vec{v} \cdot \left[\nabla \cdot \left\{ \eta \left\{ \nabla u + \{ \nabla u \}^T \right\} - pI \right\} - \rho \vec{g} \right] dV \quad (3.1)$$

Since \vec{u} is the solution of the differential equation, $\int_{\Omega} \vec{r} dV = 0$.

Rewrite equation (3.1) as

$$\int_{\Omega} \vec{v} \cdot \left[\nabla \cdot \left\{ \eta \left\{ \nabla u + \{ \nabla u \}^T \right\} \right\} \right] dV - \int_{\Omega} \vec{v} \cdot [\nabla \cdot \{ pI \}] dV - \int_{\Omega} \vec{v} \cdot \rho \vec{g} dV = 0 \quad (3.2)$$

Integrate the first integral in equation (3.2) by parts

$$\begin{aligned} \int_{\Omega} \vec{v} \cdot \left[\nabla \cdot \left\{ \eta \left\{ \nabla u + \{ \nabla u \}^T \right\} \right\} \right] dV = \\ \int_{\Gamma} \vec{v} \cdot \left\{ \eta \left\{ \nabla u + \{ \nabla u \}^T \right\} \right\} dA - \int_{\Omega} (\nabla \cdot \vec{v}) \cdot \left\{ \eta \left\{ \nabla u + \{ \nabla u \}^T \right\} \right\} dV \end{aligned} \quad (3.3)$$

where Γ specifies the boundary.

Substitute equation (3.3) into equation (3.2)

$$\begin{aligned} \int_{\Gamma} \vec{v} \cdot \left\{ \eta \left\{ \nabla u + \{\nabla u\}^T \right\} \right\} dA - \int_{\Omega} (\nabla \cdot \vec{v}) \cdot \left\{ \eta \left\{ \nabla u + \{\nabla u\}^T \right\} \right\} dV \\ - \int_{\Omega} \vec{v} \cdot [\nabla \cdot \{pI\}] dV - \int_{\Omega} \vec{v} \cdot \rho \vec{g} dV = 0 \end{aligned} \quad (3.4)$$

Integrate the third integral in equation (3.4) by parts

$$\int_{\Omega} \vec{v} \cdot [\nabla \cdot \{pI\}] dV = \int_{\Gamma} \vec{v} \cdot \{pI\} dA - \int_{\Omega} (\nabla \cdot \vec{v}) \cdot \{pI\} dV \quad (3.5)$$

Substitute equation (3.5) into equation (3.4)

$$\begin{aligned} \int_{\Gamma} \vec{v} \cdot \left\{ \eta \left\{ \nabla u + \{\nabla u\}^T \right\} \right\} dA - \int_{\Omega} (\nabla \cdot \vec{v}) \cdot \left\{ \eta \left\{ \nabla u + \{\nabla u\}^T \right\} \right\} dV \\ - \int_{\Gamma} \vec{v} \cdot \{pI\} dA + \int_{\Omega} (\nabla \cdot \vec{v}) \cdot \{pI\} dV - \int_{\Omega} \vec{v} \cdot \rho \vec{g} dV = 0 \end{aligned} \quad (3.6)$$

Rearrange this as

$$\begin{aligned} \int_{\Omega} (\nabla \cdot \vec{v}) \cdot \left\{ \eta \left\{ \nabla u + \{\nabla u\}^T \right\} \right\} dV - \int_{\Omega} (\nabla \cdot \vec{v}) \cdot \{pI\} dV \\ = - \int_{\Omega} \vec{v} \cdot \rho \vec{g} dV + \int_{\Gamma} \vec{v} \cdot \left\{ \eta \left\{ \nabla u + \{\nabla u\}^T \right\} - \{pI\} \right\} dA \end{aligned} \quad (3.7)$$

Invoking incompressibility eliminates pressure terms with the exception of specifying pressure on the boundary. The penalty method [10] is a common approximation strategy used to eliminate pressure and hence a degree of freedom that must be solved for.

The penalty method relaxes the incompressibility condition and replaces the pressure as follows [16, 20, 10]

$$p = -\Lambda \nabla \cdot \vec{u} \quad (3.8)$$

where Λ is the penalty parameter, which is a large number. The value depends on the mesh size and problem at hand, and it is generally on the order of 10^7 or 10^8 [10]. The replacement can be made with no invoking of incompressibility [16], in equation

(3.6) [10] or it can be made after integrating by parts [20]. This is reasonable because the penalty method is an approximation made to solve the problem. Substituting equation (3.8) into equation (3.7) gives

$$\begin{aligned} & \int_{\Omega} (\nabla \cdot \vec{v}) \cdot \left\{ \eta \left\{ \nabla u + \{\nabla u\}^T \right\} \right\} dV - \int_{\Omega} (\nabla \cdot \vec{v}) (\nabla \cdot \vec{u}) dV \\ &= - \int_{\Omega} \vec{v} \cdot \rho \vec{g} dV + \int_{\Gamma} \vec{v} \cdot \left\{ \eta \left\{ \nabla u + \{\nabla u\}^T \right\} - \{pI\} \right\} dA \end{aligned} \quad (3.9)$$

Note the pressure in the boundary integral must be specified and hence it remains without substitution.

3.1.2 Temperature

First we need to construct the residual error function from equation (2.31)

$$r = \frac{\partial T}{\partial t} - \frac{1}{\rho c} \nabla \cdot [k \nabla T] + \vec{u} \cdot \nabla T - \frac{Q}{\rho c}$$

where in two dimensions $r = r(x, y)$ and in three dimensions $r = r(x, y, z)$. As with the velocity weak formulation, the following derivation is in three dimensions.

To do this we multiply by a test function $v = v(x, y, z)$ and integrate over the domain Ω of the problem (i.e. volume V)

$$\int_{\Omega} r v dV = \int_{\Omega} \left(\frac{\partial T}{\partial t} - \frac{1}{\rho c} \nabla \cdot [k \nabla T] + \vec{u} \cdot \nabla T - \frac{Q}{\rho c} \right) v dV$$

As with velocity, since T is the solution of the differential equation, $\int_{\Omega} r v dV = 0$.

Substitute the identity $\nabla \cdot [v k \nabla T] = k \nabla T \cdot \nabla v + v \nabla \cdot [k \nabla T]$

$$\int_{\Omega} \left(\frac{\partial T}{\partial t} v - \frac{1}{\rho c} \nabla \cdot [v k \nabla T] + \frac{k}{\rho c} \nabla T \cdot \nabla v + v \vec{u} \cdot \nabla T - \frac{Q v}{\rho c} \right) dV = 0$$

Rearrange

$$\int_{\Omega} \left(\frac{\partial T}{\partial t} v + \frac{k}{\rho c} \nabla T \cdot \nabla v + v \vec{u} \cdot \nabla T \right) dV = \int_{\Omega} \left(\frac{1}{\rho c} \nabla \cdot [v k \nabla T] + \frac{Q v}{\rho c} \right) dV \quad (3.10)$$

Apply the divergence theorem, $\int \nabla \cdot F dV = \int F \cdot dA$, to the first integral on the right hand side

$$\int_{\Omega} \nabla \cdot [v k \nabla T] dV = \int_{\Gamma} v k \nabla T \cdot \hat{n} dA \quad (3.11)$$

where \hat{n} is the unit normal of the area, A , bounded by the volume of ice to be modeled.

In equation (3.11) use the definition of the normal derivative [4, 9], $\nabla T \cdot \hat{n} = \frac{\partial T}{\partial n}$ noting that the Geothermal heat flux at the bed is in the positive y -direction while the normal to the surface is in the negative y -direction,

$$\int_{\Gamma} vk \nabla T \cdot \hat{n} dA = \int_{\Gamma} -vk \frac{\partial T}{\partial n} dA \quad (3.12)$$

where Γ specifies the elements along the boundary, specifically the bed. Then using equation (2.34) in equation (3.12)

$$- \int_{\Gamma} vk \frac{\partial T}{\partial n} dA = \int_{\Gamma} vG dA \quad (3.13)$$

Finally substituting equation (3.13) into equation (3.10) and rearranging

$$\int_{\Omega} \frac{\partial T}{\partial t} v dV + \int_{\Omega} \frac{k}{\rho c} \nabla T \cdot \nabla v dV + \int_{\Omega} v \vec{u} \cdot \nabla T dV = \int_{\Omega} \frac{Qv}{\rho c} dV + \int_{\Gamma} \frac{vG}{\rho c} dA \quad (3.14)$$

3.2 Interpolation Functions

As previously mentioned, the Galerkin method chooses basis functions as the weight functions. Reddy [41] specifies Lagrange interpolation functions as the weight functions. Becker, Carey, and Oden [4] identify the weight functions as element shape functions that make up global basis functions. Becker, Carey, and Oden also use Lagrange functions for their element shape functions.

Basis functions must satisfy

$$\phi_i(x_j, y_j, z_j) = \begin{cases} 1, & \text{if } i = j \\ 0, & \text{if } i \neq j \end{cases} \quad (3.15)$$

where x_j , y_j , and z_j are the coordinates of node j . That is, the basis function is one at one node and zero at all the rest. The basis functions are global since each is defined over the entire finite mesh.

Globally, the approximate solutions are

$$u_x(x, y, z, t) = \sum_{i=1}^N u_x^i(t) \phi_i(x, y, z) \quad \text{and} \quad u_y(x, y, z, t) = \sum_{i=1}^N u_y^i(t) \phi_i(x, y, z) \quad (3.16)$$

$$T(x, y, z, t) = \sum_{i=1}^N T_i(t) \phi_i(x, y, z) \quad (3.17)$$

where N is the total number of nodes, u_x^i is the nodal value of u_x , u_y^i is the nodal value of u_y , T_i is the nodal value of T , and ϕ_i are the basis functions.

Locally or element-wise the approximate solutions are

$$\begin{aligned} u_x(x, y, z, t) &= \sum_{i=1}^{Ne} u_x^i(t) \psi_i^{e1}(x, y, z) \\ &\quad \text{and} \\ u_y(x, y, z, t) &= \sum_{i=1}^{Ne} u_y^i(t) \psi_i^{e1}(x, y, z) \end{aligned} \quad (3.18)$$

$$T(x, y, z, t) = \sum_{i=1}^{Ne} T_i^e(t) \psi_i^{e2}(x, y, z) \quad (3.19)$$

where Ne is the number of nodes in an element, u_x^i is the nodal value of u_x , u_y^i is the nodal value of u_y , T_i is the nodal value of T , and ψ_i^{e1} and ψ_i^{e2} are Lagrange interpolation functions. Adding local solution contributions gives the global solution. Note the unknown variables are permitted different interpolation functions. Typical Lagrange interpolation functions are linear or quadratic. In this work, all unknown variables are found using linear Lagrange interpolation functions. Hence extra identifying subscripts are dropped, that is, ψ^e is used.

3.3 Finite Element Model

The finite element model is constructed in this section using the weak form derived in section 3.1 and the approximate solution form given in section 3.2. The finite element matrices are derived.

3.3.1 Velocity

Rewrite equation (3.9) using index notation

$$\begin{aligned} \int_{\Omega} \eta v_{i,i} (u_{i,j} + u_{j,i}) dV + \int_{\Omega} \Lambda v_{i,i} u_{j,j} dV = \\ - \int_{\Omega} \rho v_i g_i dV + \int_{\Gamma} v_i (\eta (u_{i,j} + u_{j,i}) - p n_i) dA \end{aligned} \quad (3.20)$$

Find the solution on each element using equation (3.18)

$$u(x, y, z) = \sum_{i=1}^{Ne} \psi_i^e(x, y, z) u^i \quad (3.21)$$

for element e , where ψ^e is written as an $n \times l$ matrix for n dimensions and l is the dimension multiplied by the number of nodes in the element. The solution is then assembled by adding all element contributions to the solution. For example, ψ^e for a 3-dimensional problem with 4 node elements

$$\psi^e(x, y, z) = \begin{pmatrix} \psi_1^e & 0 & 0 & \psi_2^e & 0 & 0 & \psi_3^e & 0 & 0 & \psi_4^e & 0 & 0 \\ 0 & \psi_1^e & 0 & 0 & \psi_2^e & 0 & 0 & \psi_3^e & 0 & 0 & \psi_4^e & 0 \\ 0 & 0 & \psi_1^e & 0 & 0 & \psi_2^e & 0 & 0 & \psi_3^e & 0 & 0 & \psi_4^e \end{pmatrix}$$

and

$$(u^e)^T = (u_{1x}^e \quad u_{1y}^e \quad u_{1z}^e \quad u_{2x}^e \quad u_{2y}^e \quad u_{2z}^e \quad u_{3x}^e \quad u_{3y}^e \quad u_{3z}^e \quad u_{4x}^e \quad u_{4y}^e \quad u_{4z}^e)$$

Written in index notation, this becomes

$$(u_h^e)_i = \psi_{il}^e u_l^e$$

Note that the u_l are velocity components, that is, numbers.

Write the test function, Lagrange function, in index notation

$$(v_h^e)_i = \psi_{im}^e$$

where m is the problem dimension multiplied by the number of nodes in an element.

Substitute into the first integral and perform the differentiation, noting that for the matrix multiplication to make sense a transpose is needed

$$\int_{\Omega} \eta v_{i,i} (u_{i,j} + u_{j,i}) dV = \int_{\Omega} \eta \left((\psi_{im,j}^e)^T (\psi_{il,j}^e + \psi_{jl,i}^e) u_l^e \right) dV \quad (3.22)$$

Substitute into the second integral in equation (3.20) and perform the differentiation

$$\int_{\Omega} \Lambda u_{i,i} v_{i,i} dV = \int_{\Omega} \Lambda \left((\psi_{im,i}^e)^T (\psi_{il,i}^e u_l^e) \right) dV \quad (3.23)$$

Use equations (3.22) and (3.23) to define

$$k_{ij}^e = \int_{\Omega} \left(\eta (\psi_{im,j}^e)^T (\psi_{il,j}^e + \psi_{jl,i}^e) + \Lambda \left((\psi_{im,i}^e)^T (\psi_{il,i}^e) \right) \right) dV \quad (3.24)$$

Substitute into the third integral in equation (3.20)

$$\int_{\Omega} \rho v_i g_i dV = \int_{\Omega} \rho (\psi_{im}^e)^T g_i dV$$

Define

$$(f_1)_i^e = \int_{\Omega} \rho (\psi_{im}^e)^T g_i dV \quad (3.25)$$

Substitute into the remaining integrals

$$\int_{\Gamma} v_i (\eta (u_{i,j} + u_{j,i}) - p n_i) dA = \int_{\Gamma} \eta (\psi_{il,j}^e + \psi_{jl,i}^e) - (\psi_{im}^e)^T p n_i dA$$

Define

$$(f_2)_i^e = \int_{\Gamma} \eta (\psi_{il,j}^e + \psi_{jl,i}^e) - (\psi_{im}^e)^T p n_i dA \quad (3.26)$$

Using equations (3.25), and (3.26) define

$$f_i^e = -(f_1)_i^e + (f_2)_i^e \quad (3.27)$$

The local solutions are

$$\sum_{j=1}^{Ne} k_{ij}^e u_j = f_i^e \quad i = 1, 2, 3, \dots, Ne \quad (3.28)$$

where Ne is the number of nodes in an element.

The global solution is

$$\sum_{j=1}^N K_{ij} u_j = F_i \quad i = 1, 2, 3, \dots, N \quad (3.29)$$

where

$$K_{ij} = \sum_{e=1}^E k_{ij}^e \quad i, j = 1, 2, 3, \dots, N \quad (3.30)$$

and

$$F_i = \sum_{e=1}^E f_i^e \quad i = 1, 2, 3, \dots, N \quad (3.31)$$

where E is the number of elements, and N is the total number of nodes in the domain.

3.3.2 Temperature

Expand equation (3.14)

$$\begin{aligned} & \int_{\Omega} \frac{\partial T}{\partial t} v \, dV \\ & + \int_{\Omega} \left[\frac{k}{\rho c} \left(\frac{\partial T}{\partial x} \frac{\partial v}{\partial x} + \frac{\partial T}{\partial y} \frac{\partial v}{\partial y} + \frac{\partial T}{\partial z} \frac{\partial v}{\partial z} \right) + v \left(u_x \frac{\partial T}{\partial x} + u_y \frac{\partial T}{\partial y} + u_z \frac{\partial T}{\partial z} \right) \right] dV \\ & = \int_{\Omega} \frac{Qv}{\rho c} \, dV + \int_{\Omega} \frac{vG}{\rho c} \, dA \end{aligned} \quad (3.32)$$

The temperature solution T_h has the form

$$T_h(x, y, z, t) = \sum_{j=1}^N T_j(t) \phi_j(x, y, z) \quad (3.33)$$

where N is the total number of nodes in the domain, T_j is the temperature at a node, and ϕ_j is the basis function that satisfies equation (3.15). The test function in a typical element, v_h , has a similar form

$$v_h(x, y, z) = \sum_{i=1}^N v_i \phi_i(x, y, z) \quad (3.34)$$

except that it is independent of time. Substituting into the first integral

$$\int_{\Omega} \frac{\partial T}{\partial t} v dV = \int_{\Omega} \left(\sum_{j=1}^N \frac{dT_j}{dt} \phi_j \right) \left(\sum_{i=1}^N v_i \phi_i \right) dV.$$

Absorb constants v_i into constants T_j by letting v_i equal one for one node with number i and zero for the rest of the nodes. Then interchanging the summation and integration

$$\int_{\Omega} \frac{\partial T}{\partial t} v dV = \sum_{j=1}^N \left(\int_{\Omega} \phi_i \phi_j dV \right) \frac{dT_j}{dt} \quad i = 1, 2, \dots, N$$

Define

$$C_{ij} = \int_{\Omega} \phi_i \phi_j dV \quad i, j = 1, 2, \dots, N.$$

Then the first integral is written as

$$\int_{\Omega} \frac{\partial T}{\partial t} v dV = \sum_{j=1}^N C_{ij} \frac{dT_j}{dt} \quad i = 1, 2, \dots, N.$$

C_{ij} is known as the capacitance matrix.

Following the same procedure, the second integral is

$$\begin{aligned} & \int_{\Omega} \left[\frac{k}{\rho c} \left(\frac{\partial T}{\partial x} \frac{\partial v}{\partial x} + \frac{\partial T}{\partial y} \frac{\partial v}{\partial y} + \frac{\partial T}{\partial z} \frac{\partial v}{\partial z} \right) + v \left(u_x \frac{\partial T}{\partial x} + u_y \frac{\partial T}{\partial y} + u_z \frac{\partial T}{\partial z} \right) \right] dV \\ &= \sum_{j=1}^N \int_{\Omega} \left[\frac{k}{\rho c} \left(\frac{\partial \phi_i}{\partial x} \frac{\partial \phi_j}{\partial x} + \frac{\partial \phi_i}{\partial y} \frac{\partial \phi_j}{\partial y} + \frac{\partial \phi_i}{\partial z} \frac{\partial \phi_j}{\partial z} \right) + \phi_i \left(u_x \frac{\partial \phi_j}{\partial x} + u_y \frac{\partial \phi_j}{\partial y} + u_z \frac{\partial \phi_j}{\partial z} \right) \right] dV T_j \\ & \quad i = 1, 2, \dots, N. \end{aligned}$$

Note that the second integral contains conduction and advection terms. The velocity components are values at the integration points. That is, integrate the velocity components instead of treating them as constant over the element. Define

$$K_{ij} = \int_{\Omega} \left[\frac{k}{\rho c} \left(\frac{\partial \phi_i}{\partial x} \frac{\partial \phi_j}{\partial x} + \frac{\partial \phi_i}{\partial y} \frac{\partial \phi_j}{\partial y} + \frac{\partial \phi_i}{\partial z} \frac{\partial \phi_j}{\partial z} \right) + \phi_i \left(u_x \frac{\partial \phi_j}{\partial x} + u_y \frac{\partial \phi_j}{\partial y} + u_z \frac{\partial \phi_j}{\partial z} \right) \right] dV$$

$i, j = 1, 2, \dots, N.$

which is known as the stiffness matrix, so named for the engineering origins of finite element methods. The second integral becomes

$$\begin{aligned} \int_{\Omega} \left[\frac{k}{\rho c} \left(\frac{\partial T}{\partial x} \frac{\partial v}{\partial x} + \frac{\partial T}{\partial y} \frac{\partial v}{\partial y} + \frac{\partial T}{\partial z} \frac{\partial v}{\partial z} \right) + v \left(u_x \frac{\partial T}{\partial x} + u_y \frac{\partial T}{\partial y} + u_z \frac{\partial T}{\partial z} \right) \right] dV \\ = \sum_{j=1}^N K_{ij} T_j \quad i = 1, 2, \dots, N. \end{aligned}$$

The source term integrals are rewritten following the same procedure

$$\int_{\Omega} \frac{Qv}{\rho c} dV + \int_{\Omega} \frac{vG}{\rho c} dA = \int_{\Omega} \frac{Q}{\rho c} \phi_i dV + \int_{\Omega} \frac{G}{\rho c} \phi_i dA \quad i = 1, 2, \dots, N.$$

Define

$$F_i^1 = \int_{\Omega} \frac{Q}{\rho c} \phi_i dV$$

and

$$F_i^2 = \int_{\Omega} \frac{G}{\rho c} \phi_i dA.$$

Then

$$\int_{\Omega} \frac{Qv}{\rho c} dV + \int_{\Omega} \frac{vG}{\rho c} dA = F_i^1 + F_i^2.$$

Equation (3.32) is rewritten as

$$\sum_{j=1}^N \left(C_{ij} \frac{dT_j}{dt} + K_{ij} T_j \right) = F_i^1 + F_i^2 \quad i = 1, 2, \dots, N \quad (3.35)$$

noting, as defined earlier, that the sum j is over nodes in an element; there is one equation for each node i . The right hand side is known as the load vector.

Comparison of equations (3.17) and (3.19) shows they have the same form. Hence the local solution is written by relacing ϕ with ψ and summing appropriately.

3.4 Upwinding

The Galerkin approximation employs symmetry of matrices, a space saving “must” in computer computations. However, convection and advection type terms

ruin the symmetry when adding terms to the matrices. The presence of convection and advection causes oscillations which corrupt the solutions [10]. Creating finer and finer meshes until the oscillations go away is one way to solve the problem [10] but this is not practical in most cases due to memory constraints. Stabilization techniques quiet the noise so that the true solution may be found.

Following streamline upwind presented in [10] we replace equation (3.32)

$$\begin{aligned} & \int_{\Omega} \frac{\partial T}{\partial t} v \, dV \\ & + \int_{\Omega} \left[\frac{k}{\rho c} \left(\frac{\partial T}{\partial x} \frac{\partial v}{\partial x} + \frac{\partial T}{\partial y} \frac{\partial v}{\partial y} + \frac{\partial T}{\partial z} \frac{\partial v}{\partial z} \right) + v \left(u_x \frac{\partial T}{\partial x} + u_y \frac{\partial T}{\partial y} + u_z \frac{\partial T}{\partial z} \right) \right] dV \\ & = \int_{\Omega} \frac{Qv}{\rho c} \, dV + \int_{\Omega} \frac{vG}{\rho c} \, dA \end{aligned}$$

with

$$\begin{aligned} & \int_{\Omega} \frac{\partial T}{\partial t} v \, dV \\ & + \int_{\Omega} \left[\left(\frac{k}{\rho c} + \beta \frac{u_x L}{2} \right) \frac{\partial T}{\partial x} \frac{\partial v}{\partial x} + \frac{k}{\rho c} \left(\frac{\partial T}{\partial y} \frac{\partial v}{\partial y} + \frac{\partial T}{\partial z} \frac{\partial v}{\partial z} \right) + v \left(u_x \frac{\partial T}{\partial x} + u_y \frac{\partial T}{\partial y} + u_z \frac{\partial T}{\partial z} \right) \right] dV \\ & = \int_{\Omega} \frac{Qv}{\rho c} \, dV + \int_{\Omega} \frac{vG}{\rho c} \, dA \end{aligned}$$

where L is the characteristic length, $\beta = \coth \text{Pe} - \frac{1}{\text{Pe}}$, with Peclet number, Pe as discussed in section 2.4.6. Note that upwinding is added only in the flow direction.

Rearrange as

$$\begin{aligned} & \int_{\Omega} \frac{\partial T}{\partial t} v \, dV \\ & + \int_{\Omega} \left[\frac{k}{\rho c} \left(\frac{\partial T}{\partial x} \frac{\partial v}{\partial x} + \frac{\partial T}{\partial y} \frac{\partial v}{\partial y} + \frac{\partial T}{\partial z} \frac{\partial v}{\partial z} \right) + \left(v + \beta \frac{L}{2} \frac{\partial v}{\partial x} \right) u_x \frac{\partial T}{\partial x} + v \left(u_y \frac{\partial T}{\partial y} + u_z \frac{\partial T}{\partial z} \right) \right] dV \\ & = \int_{\Omega} \frac{Qv}{\rho c} \, dV + \int_{\Omega} \frac{vG}{\rho c} \, dA \end{aligned}$$

Only the second integral has changed. Use the procedure of section 3.3.2 to write

$$\int_{\Omega} \left[\frac{k}{\rho c} \left(\frac{\partial T}{\partial x} \frac{\partial v}{\partial x} + \frac{\partial T}{\partial y} \frac{\partial v}{\partial y} + \frac{\partial T}{\partial z} \frac{\partial v}{\partial z} \right) + \left(v + \beta \frac{L}{2} \frac{\partial v}{\partial x} \right) u_x \frac{\partial T}{\partial x} + v \left(u_y \frac{\partial T}{\partial y} + u_z \frac{\partial T}{\partial z} \right) \right] dV$$

$$\begin{aligned}
&= \sum_{j=1}^N \int_{\Omega} \left[\frac{k}{\rho c} \left(\frac{\partial \phi_i}{\partial x} \frac{\partial \phi_j}{\partial x} + \frac{\partial \phi_i}{\partial y} \frac{\partial \phi_j}{\partial y} + \frac{\partial \phi_i}{\partial z} \frac{\partial \phi_j}{\partial z} \right) + \left(\phi_i + \beta \frac{L}{2} \frac{\partial \phi_i}{\partial x} \right) \left(u_x \frac{\partial \phi_j}{\partial x} \right) \right. \\
&\quad \left. + \phi_i \left(u_y \frac{\partial \phi_j}{\partial y} + u_z \frac{\partial \phi_j}{\partial z} \right) \right] dV T_j \quad i = 1, 2, \dots, N.
\end{aligned}$$

3.5 Elements

The finite element mesh consists of the elements covering the problem domain. The first step in constructing the finite element mesh is to subdivide the problem domain into a finite number of elements. The elements cover the entire domain but do not overlap. In two dimensions the elements are usually triangular or quadrilateral, and in three dimensions bricks are commonly used. Quadrilateral elements usually have four-, eight-, or nine-nodes. They can have a single node or more than nine-nodes. To simplify calculations, the nodes are evenly spaced in the element. For example the four-node quadrilateral has a node in each of the four corners. A brick will usually have eight-nodes, but may have more or less. Adjacent elements share nodes in the finite element mesh. Other element shapes may be used. Combinations of different shaped elements may also subdivide the domain.

A master element, $\hat{\Omega}$, simplifies calculations. Typically in two dimensions the element shape is a four-, eight-, or nine-node quadrilateral, but the master element is a square with the same number of nodes (isoparametric case), fewer nodes (subparametric case), or more nodes (superparametric case) than the element shape. Cartesian coordinates, x, y, z locate points within the generic element Ω_e , and local coordinates, ξ, η , and ζ locate points in the master element $\hat{\Omega}$. The local coordinates typically range from -1 to $+1$ whereas the Cartesian coordinates could take any values. An element map T_e (not to be confused with temperature T) transforms from local coordinates to Cartesian coordinates using the master shape functions

$\hat{\psi}_i$; that is, T_e maps $\hat{\Omega}$ onto Ω_e [4].

$$T_e : \left. \begin{aligned} x &= x(\xi, \eta, \zeta) = \sum_{j=1}^N x_j \hat{\psi}_j(\xi, \eta, \zeta) \\ y &= y(\xi, \eta, \zeta) = \sum_{j=1}^N y_j \hat{\psi}_j(\xi, \eta, \zeta) \\ z &= z(\xi, \eta, \zeta) = \sum_{j=1}^N z_j \hat{\psi}_j(\xi, \eta, \zeta) \end{aligned} \right\}$$

The map also has requirements that must be satisfied. It must be invertible, meaning coordinates can be transformed from Cartesian to local. As a result, an element is suitable if no interior angles are greater than 180° . Mathematically, the determinant of the Jacobian $|J|$ of the transformation T_e must be positive everywhere [4]

$$|J| = \begin{vmatrix} \frac{\partial x}{\partial \xi} & \frac{\partial x}{\partial \eta} & \frac{\partial x}{\partial \zeta} \\ \frac{\partial y}{\partial \xi} & \frac{\partial y}{\partial \eta} & \frac{\partial y}{\partial \zeta} \\ \frac{\partial z}{\partial \xi} & \frac{\partial z}{\partial \eta} & \frac{\partial z}{\partial \zeta} \end{vmatrix}$$

In addition, the mapping must generate a mesh with no gaps but also with no overlapping. For example, the shape functions for a 4-node quadrilateral master element are

$$\begin{aligned} \hat{\psi}_1 &= \frac{1}{4}(1 - \xi)(1 - \eta) \\ \hat{\psi}_2 &= \frac{1}{4}(1 + \xi)(1 - \eta) \\ \hat{\psi}_3 &= \frac{1}{4}(1 + \xi)(1 + \eta) \\ \hat{\psi}_4 &= \frac{1}{4}(1 - \xi)(1 + \eta). \end{aligned}$$

The model requires a surface and bed. The mesh is constructed by dividing the thickness into a specified uniform number of nodes. Quadrilateral elements are formed between adjacent rows, starting at the left edge.

3.6 Integrating

Computing the integrals in section 3.3 gives the local (i.e. element) solutions. Gaussian quadrature is a standard method used in FEM to compute such integrals

[4]. Gaussian quadrature works by evaluating each interpolation function as well as derivatives of the interpolation functions in an element at specified locations within the element. Next, the interpolation functions evaluated at the specific integration points are multiplied by an appropriate weight function. Finally, sum the results over all of the integration points. Gaussian quadrature has specific integration points and weights. The number of points used in the rule determines the order of the rule. It is well known that for Gaussian quadrature of order N determines exactly a polynomial of degree $(2N - 1)$ [4].

3.7 The Solver

The solution is found using the matrices given in section 3.3. Local (i.e. element) contributions are assembled into the global matrix. Next the boundary conditions are applied. The final step is to solve the system of equations written in matrix form. This work uses standard Gaussian elimination and back substitution.

3.8 Picard Method

The coupling of the momentum and thermodynamic solutions along with material nonlinearity makes iteration necessary. The iteration algorithm used is the Picard method, a direct iteration procedure. With the Picard method, computation of the new solution uses the old or previous solution. Iteration continues until the solution converges.

3.8.1 Velocity Convergence Test

A convergence test indicates if the solution has converged. The following convergence test [41] is used

$$\sqrt{\frac{\sum_{i=1}^N \left(u_i^{(r)} - u_i^{(r-1)}\right)^2}{\sum_{i=1}^N \left(u_i^{(r)}\right)^2}} < \epsilon \quad (3.36)$$

where N is the number of nodes, u_i is velocity magnitude at a node, r is the iteration number, and ϵ is the tolerance, a small number. The convergence test is performed after each iteration.

3.8.2 Temperature Convergence Test

The temperature equation has mild nonlinearity in the conduction term. That is, thermal conductivity depends weakly on temperature. The specific heat also depends on temperature. Hence a different convergence test is needed in solving for temperature. The stiffness matrix and load vector are reset for any new temperatures above the pressure melting point. The system is re-solved. This process is repeated until all new values are at or below the pressure melting point.

3.8.3 Convergence Acceleration Parameter

For each iteration, the current solution is stored for use in finding the next solution. This solution can be accepted unconditionally or, to speed up convergence, it can be combined with the previous solution and stored. The convergence acceleration parameter specifies the percentage of previous and current solutions to be incorporated into the next trial solution. For example,

$$\eta = (CAP)\eta^{(r-1)} + (1 - CAP)\eta^{(r)} \quad (3.37)$$

where CAP is the convergence acceleration parameter, η is the linearization term incorporated into the next trial solution, and r is the iteration number. Note the convergence acceleration parameter takes values $0 \leq CAP < 1$. This work tunes the convergence acceleration parameter for monotonic convergence, which is faster than oscillatory convergence.

Chapter 4

RESULTS

In this chapter I present the results of the nonlinear solution including our slippery layer approach. The first section contains program verification. The experimental setups are given and a number of domains are tested. The second section shows results for an application of the model to a real world ice stream, namely Whillans Ice Stream.

4.1 Verification

A number of studies and tests are performed to verify the model. Verification consists of three different kinds of tests, namely sensitivity studies, comparison with known analytical approximations, and testing of thermodynamic configurations. Sensitivity studies of the resolution, the effect of aspect ratio, tolerance level and convergence acceleration parameter are performed. The known analytical approximations include the shallow ice approximation and Weertman thinning rate. Three different thermodynamic situations are setup and tested. Results are presented for each test performed.

4.1.1 Experiment Setups

The following discusses the different experiment setups used in model runs. Each model run requires input data. The input data contains measured surface and bed information, accumulation rate, and surface temperatures, if available. If surface temperature measurements are not available then equation (2.33) is used. Repeated here for convenience,

$$T = T_0 + \gamma y_e$$

where $T_{base} = -30$ °C is the base temperature, and $\gamma = -6.5$ °C km⁻¹ is the lapse rate, and y_e is the elevation in kilometers (km). The experiment parameters are number of rows of nodes, temperature boundary conditions, velocity boundary conditions, convergence acceleration parameter, and tolerance. The input determines the number of columns of nodes. The output is the number of elements, aspect ratio, velocity, temperature, strain rate, deviatoric stress, pressure, strain heating, Peclet number, and linearization term, $B\dot{\varepsilon}_e^{frac{1-nn}}$, discussed in section 2.3.3.

Table 4.1 summarizes experiment setup A performed with the model on various domains.

Parameter		
Number of Elements		Tested Quantity
Convergence Acceleration Parameter		Tested Quantity
Tolerance		Tested Quantity
Boundary Condition		
Velocity	Surface	Free
	Left End, at Grounding Line	Pressure due to ice resolved into cryostatic force
	Right End, Inland	Pressure due to ice resolved into cryostatic force
	Bed	Zero Velocity
Temperature	Isothermal	-25 °C

Table 4.1: Experiment A setup.

Table 4.2 summarizes the experiments performed with the model for a floating slab of ice. Note that the velocity must be specified in at least one location along the bed since otherwise the solution varies by a constant.

Parameter		
Number of Elements		Tested Quantity
Convergence Acceleration Parameter		Tested Quantity
Tolerance		Tested Quantity
Boundary Condition		
Velocity	Surface	Free
	Left End, at Grounding Line	Pressure due to water resolved into hydrostatic force
	Right End, Inland	Pressure due to water resolved into hydrostatic force
	Bed	Zero y component Zero x component at $x = 0$
Temperature	Isothermal	-10 °C

Table 4.2: Experiment B setup.

Table 4.3 summarizes experiments performed with the model using Whillans Ice Stream as the problem domain.

Parameter		
Number of Elements		Tested Quantity
Convergence Acceleration Parameter		Tested Quantity
Tolerance		Tested Quantity
Boundary Condition		
Velocity	Surface	Free
	Left End, at Grounding Line	Pressure due to water resolved into force
	Right End, Inland	Pressure due to ice resolved into force
	Bed	Zero Velocity
Temperature	Surface	Temperature due to measurement or equation (2.33)
	Bed	Geothermal Flux of $3.17 \times 10^5 \text{ cal a}^{-1} \text{ m}^{-2}$, equivalent to 42 mW m^{-2}

Table 4.3: Experiment C setup.

4.1.2 Rectangular Domain

The velocity solution is sensitive to the resolution of the mesh and the aspect ratio. Aspect ratio is the ratio of the element width to height. The effects of mesh resolution and the aspect ratio can be teased apart for a rectangular domain. A rectangular glacier allows one to hold the mesh resolution constant while varying the aspect ratio by adding or removing columns or rows. A rectangular domain also allows one to hold the aspect ratio constant while varying the mesh resolution; for example, one can set the number of rows of nodes equivalent to the number of columns of nodes and then vary the number of columns per run.

Imbalance of force applied at the sides or the presence of surface slopes are two conditions that cause velocity in ice. Hence a rectangular domain will have zero velocity. However, a profile such as a parallelogram with parallel surface and bed, and parallel sides will have nonzero velocity while allowing either the mesh resolution or the aspect ratio to be held constant while varying the other.

The first set of tests probes the mesh resolution. Consider the domain described by

$$\begin{aligned}y_{\text{surface}} &= 0.0015x + 1000 \\ y_{\text{bed}} &= 0.0015x\end{aligned}\tag{4.1}$$

where $0 \leq x \leq 1,000$. This describes a 1000 m thick glacier on a bed with a slope of 0.0015, the average slope of Whillans Ice Stream. In this set of tests, experiment setup A is used, see Table 4.1. The aspect ratio is held at 1 by setting the number of rows equal to the number of columns. For each test the system runs until equilibrium is reached using the convergence test given in equation (3.36) with a tolerance of 0.001. The convergence acceleration parameter given by equation (3.37) is set at 0.0.

Table 4.4 lists the run, and the mesh resolution being tested. The number of elements in a column and the number of elements in the domain serve as metrics of the mesh resolution.

Run	Number of elements per column	Number of elements
(a)	5	25
(b)	10	100
(c)	25	625
(d)	50	2500

Table 4.4: List of mesh resolution metrics tested. The model is run with the domain given in equation (4.1) using experiment setup A, given in Table 4.1. The tolerance is 0.001 and the convergence acceleration parameter is 0.0. The aspect ratio is 1 for each test.

Figure 4.1 shows the node configurations of the mesh resolutions listed in Table 4.4. The nodes, and hence elements, are equally spaced in the x - and y -directions where the origin is in the lower left corner of the problem domain specified by equation (4.1). The number of columns is read in from the input file. The number of rows is set equal to the number of columns. The number of nodes is found by multiplying the number of rows and columns. Two rows and two columns are required to make an element. Hence, the number of elements is found by multiplying the number of rows minus one and the number of columns minus one. Note the number of elements in a column of elements is the number of rows of nodes minus one since two rows of nodes are required to make an element.

Figure 4.2 shows the x -component of the velocity of the system described by equation (4.1). Figure 4.2 (a) shows the test system with 25 elements total with 5 elements per column. Figure 4.2 (b) shows the test system with 100 elements total with 10 elements per column. Figure 4.2 (c) shows the test system with 625 elements total with 25 elements per column. Figure 4.2 (d) shows the test system with 2500

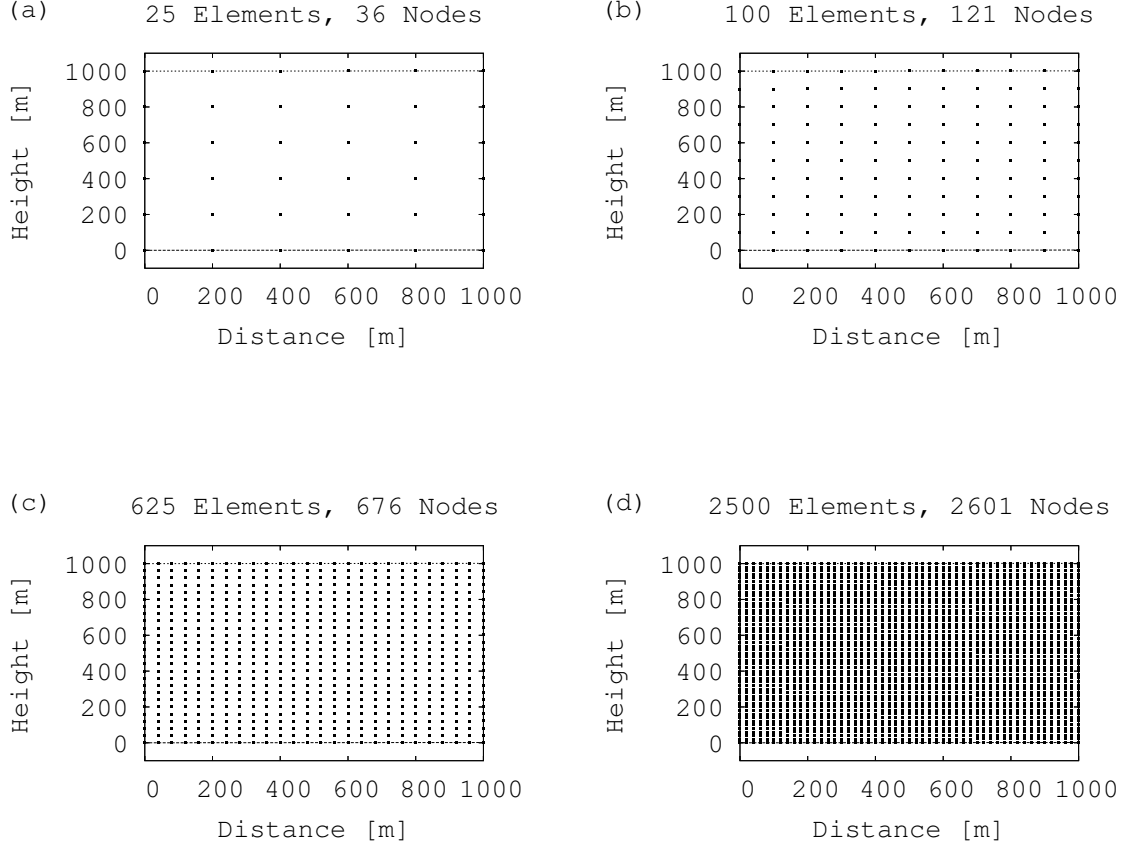


Figure 4.1: Testing the number of elements, domain with nodes. The aspect ratio is held constant at 1. The model is run with the domain given in equation (4.1) using experiment setup A. The tolerance is $1e - 3$ and the convergence acceleration parameter is 0.0. The domain with nodes for (a) 25 elements total with 5 elements per column (b) 100 elements total with 10 elements per column. (c) 625 elements total with 25 elements per column. (d) 2500 elements total with 50 elements per column.

elements total with 50 elements per column. The solution has the same general form in each test as shown in the figure. The values of the velocity magnitude change most in going from 25 elements to 100 elements. The values of the velocity magnitude change very little in going from 100 elements to 625 elements, and there is almost no change in going from 625 elements to 2500 elements.

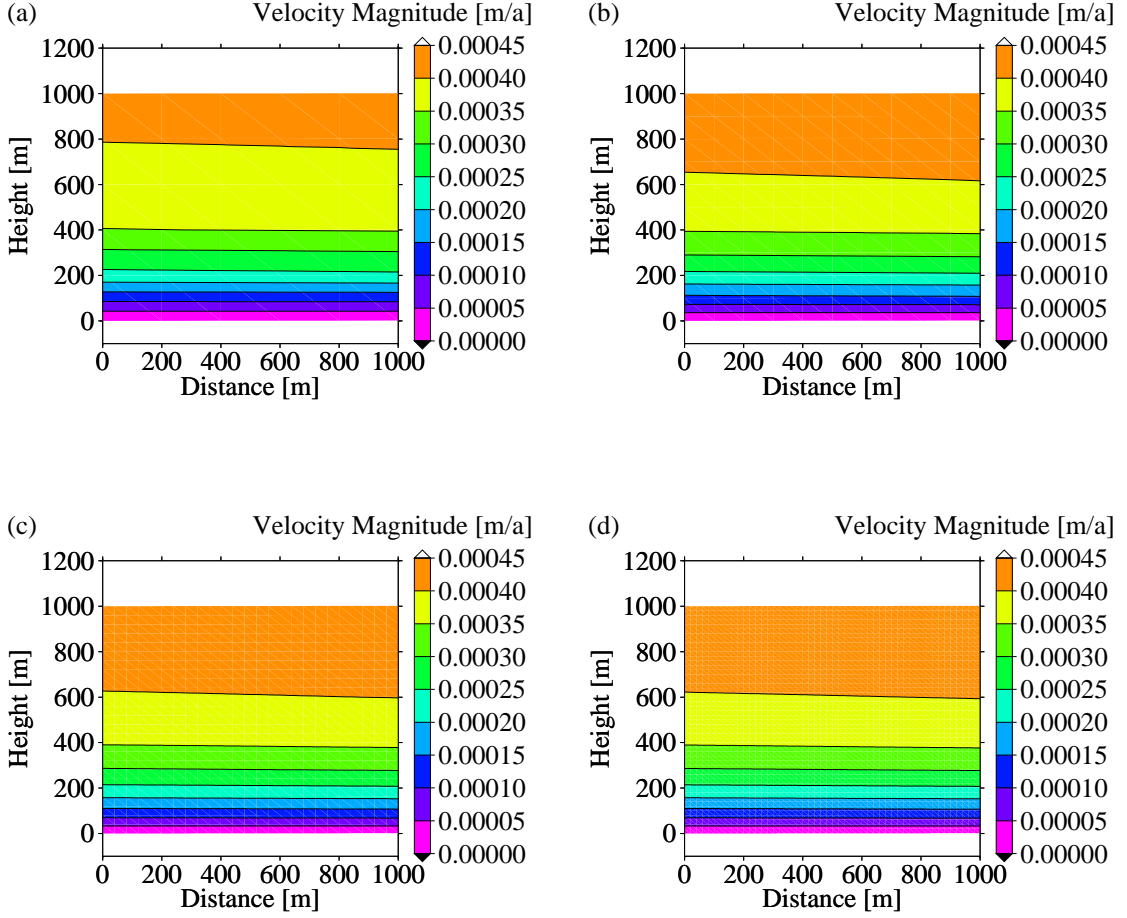


Figure 4.2: Testing the mesh resolution. The aspect ratio is held constant at 1. The model is run with the domain given in equation (4.1) using experiment setup A. The convergence acceleration parameter is 0.0 and the tolerance is $1e - 3$. (a) 25 elements total with 5 elements per column (b) 100 elements total with 10 elements per column. (c) 625 elements total with 25 elements per column. (d) 2500 elements total with 50 elements per column.

The aspect ratio tests also use the domain described by equations (4.1). Experiment setup A is used, see Table 4.1. Each test has 2500 elements. For each test the system runs until equilibrium is reached using the convergence test given in equation (3.36) with a tolerance of $1e - 3$. The convergence acceleration parameter given by equation (3.37) is set at 0.0.

Table 4.5 lists the number of elements per column, the number of columns, and the different aspect ratios tested.

Run	Number of elements per column	Number of columns	Maximum Aspect Ratio
(a)	1250	2	625
(b)	500	5	100
(c)	250	10	25
(d)	50	50	1

Table 4.5: List of aspect ratios tested. The model is run with the domain given in equation (4.1) using experiment setup A, given in Table 4.1. Each run uses the convergence test given in equation (3.36) with a tolerance of $1e - 3$. The convergence acceleration parameter is 0.0. Each test has 2500 elements.

Figure 4.3 shows the node configurations for the runs listed in Table 4.5. The figure shows the node column spacing is uniform and the node row spacing is uniform. The node column spacing is different from the node row spacing with the exception of (d). As the number of columns increases, the aspect ratio decreases. In (a) through (c) only the first 10 m in the vertical is shown in order to show the nodes due to the close spacing in the columns.

Figure 4.4 shows the velocity magnitude as a function of depth for the system described by equation (4.1) for aspect ratios of 1, 25, and 625. The velocity magnitude curves correspond to the aspect ratios listed in Table 4.5. Each curve is taken from the middle of the system, at $x = 500$ m. Figure 4.4 (a) shows the curves are very close in value, mostly overlapping. Figure 4.4 (b) shows the values are different near the surface of the system in the second and third significant digits. The figure also shows the values range from 0.000410 to 0.000413 with a maximum difference of 0.78%. As the aspect ratio gets larger, the model overestimates the values of the velocity magnitude in areas where it is moving fastest. Note that the system tested, equation (4.1), has very low surface slope ($\alpha = 0.0015$) and experiment setup A,

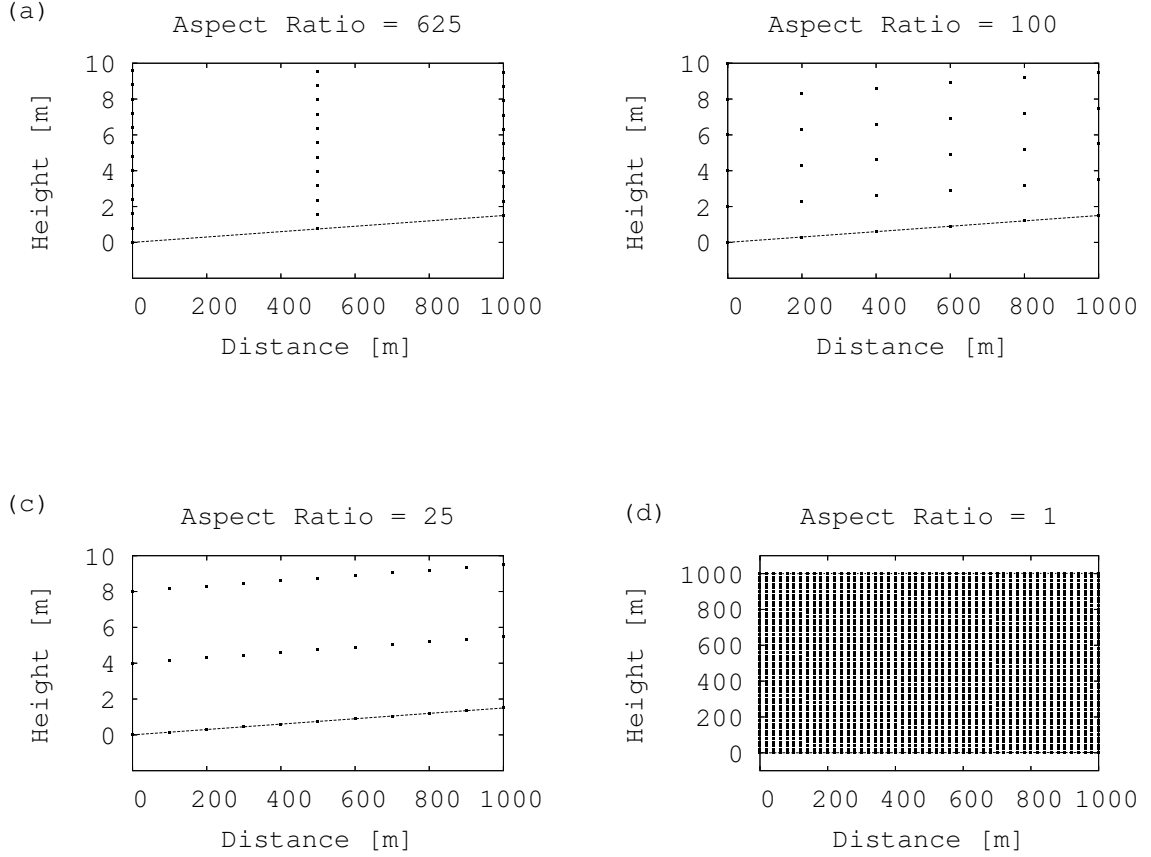


Figure 4.3: Testing the aspect ratio, domain with nodes. The number of elements is held constant at 2500. The model is run with the domain given in equation (4.1) using experiment setup A. The tolerance is $1e - 3$ and the convergence acceleration parameter is 0.0. The domain with nodes for (a) 1250 elements per column in 2 columns (b) 500 elements column in 5 columns. (c) 250 elements per column in 10 columns. (d) 50 elements per column in 50 columns.

(Table 4.1) has zero velocity specified at the bed, hence the velocities are also low. This test shows aspect ratio affects the results even at low velocities.

Figure 4.5 shows the velocity magnitude as a function of depth for the system described by equation (4.1) for aspect ratios of 1, 25, and 100. As in Figure 4.4 the velocity magnitude curves correspond to the aspect ratios listed in Table 4.5. Each velocity magnitude curve is taken at $x = 400$ m. As with the previous aspect ratio test, Figure 4.5 (a) shows the curves are very close in value and mostly overlap. Figure 4.5 (b) shows the values differ near the surface of the system where the

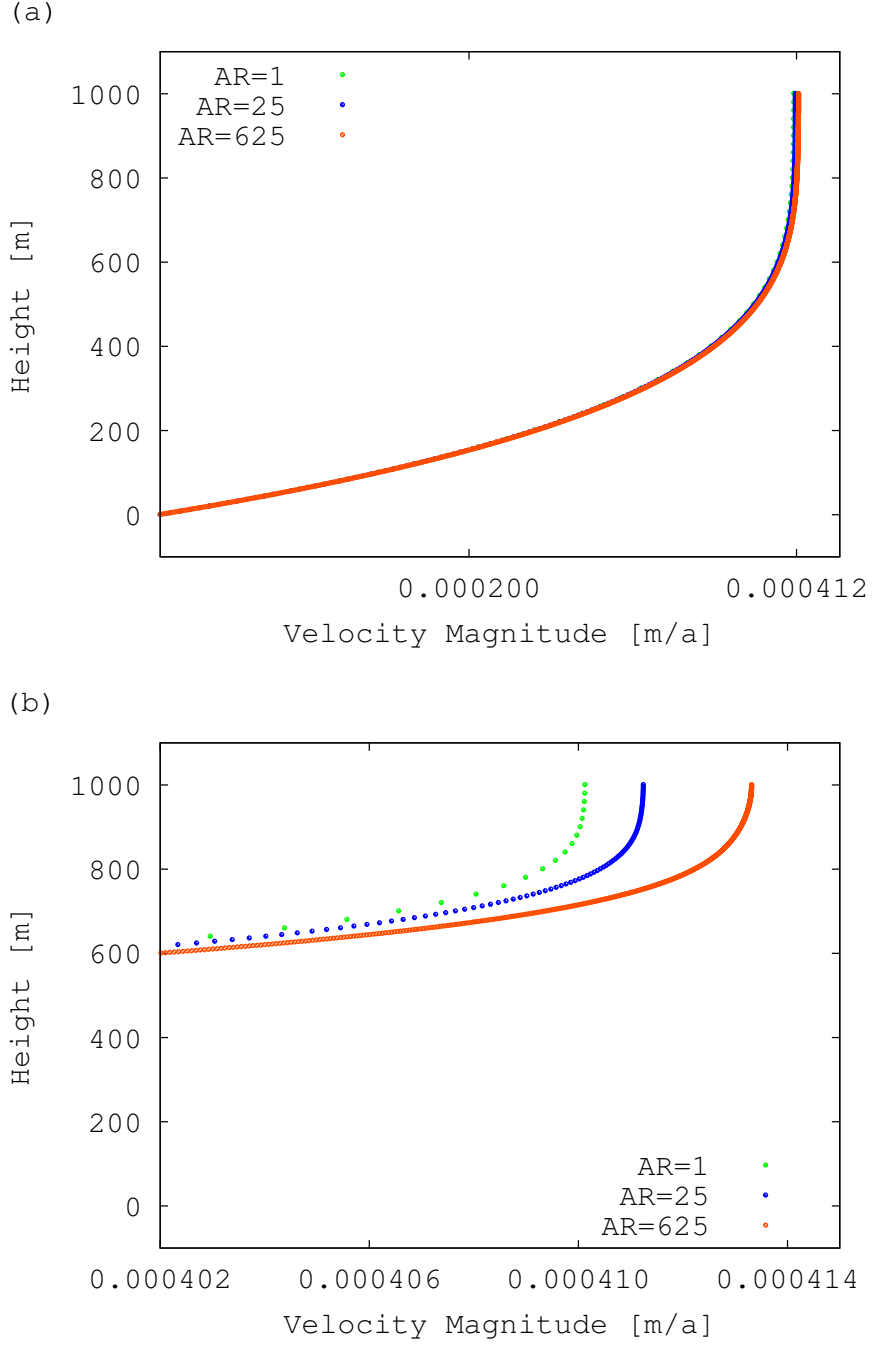


Figure 4.4: Testing the aspect ratio. The number of elements is held constant at 2500. The model is run with the domain given in equation (4.1) using experiment setup A. Each run uses the convergence test in equation (3.36) with a tolerance of $1e-3$. The convergence acceleration parameter is 0.0. (a) the velocity magnitude at $x = 500$ m, (b) horizontal scale adjusted to show the differences in velocity magnitude for the different aspect ratios tested.

velocity magnitude is greatest. At the surface the maximum difference in velocity magnitude is 0.51%.

In the final sensitivity study, I investigate both the tolerance level and convergence acceleration parameter. The domain described by equation (4.1) is used. The test uses experiment setup A, see Table 4.1. As with the other sensitivity tests, the system runs until equilibrium is reached using the convergence test given in equation (3.36). Each test system consists of 2500 elements and the aspect ratio is 1.

Results are presented in Figure 4.6. The systems converged to the solutions shown. Comparison of the velocity magnitude profile for systems with different tolerance levels shows similar solution shape. Figure 4.6 (a) shows solutions nearly overlap for tolerances of $1e-2$ to $1e-7$. Figure (b) shows the values range from $0.0004096 \text{ m a}^{-1}$ to $0.0004134 \text{ m a}^{-1}$ for tolerances of $1e-7$ to $1e-2$ respectively. The gain in precision in the solution in going from $1e-3$ to $1e-7$ is only 0.012%.

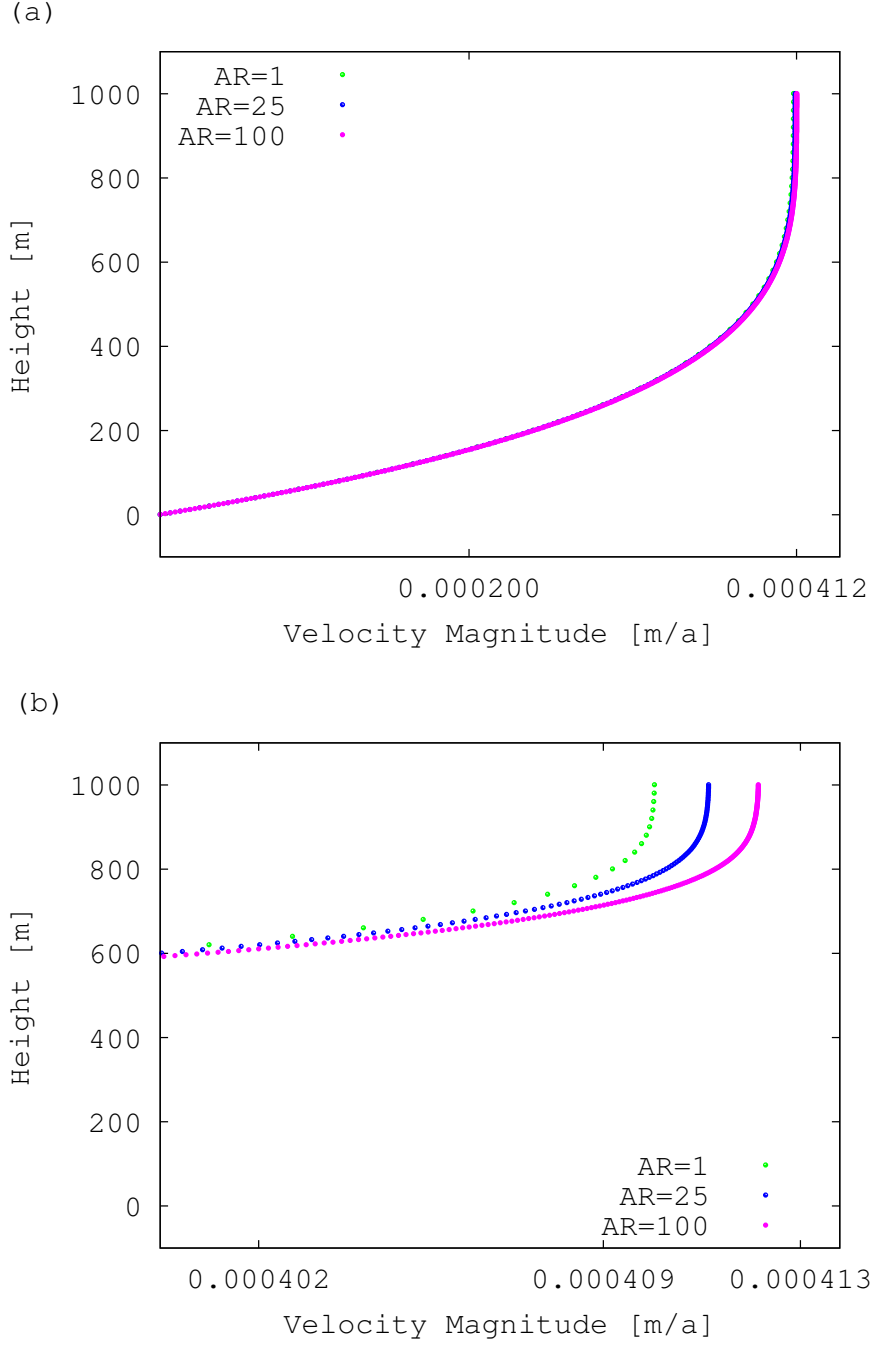


Figure 4.5: Testing the aspect ratio. The number of elements is held constant at 2500. The model is run with the domain given in equation (4.1) using experiment setup A. Each run uses the convergence test in equation (3.36) with a tolerance of 0.001. The convergence acceleration parameter is 0.0. (a) the velocity magnitude at $x = 400$ m, (b) horizontal scale adjusted to show the differences in velocity magnitude for the different aspect ratios tested.

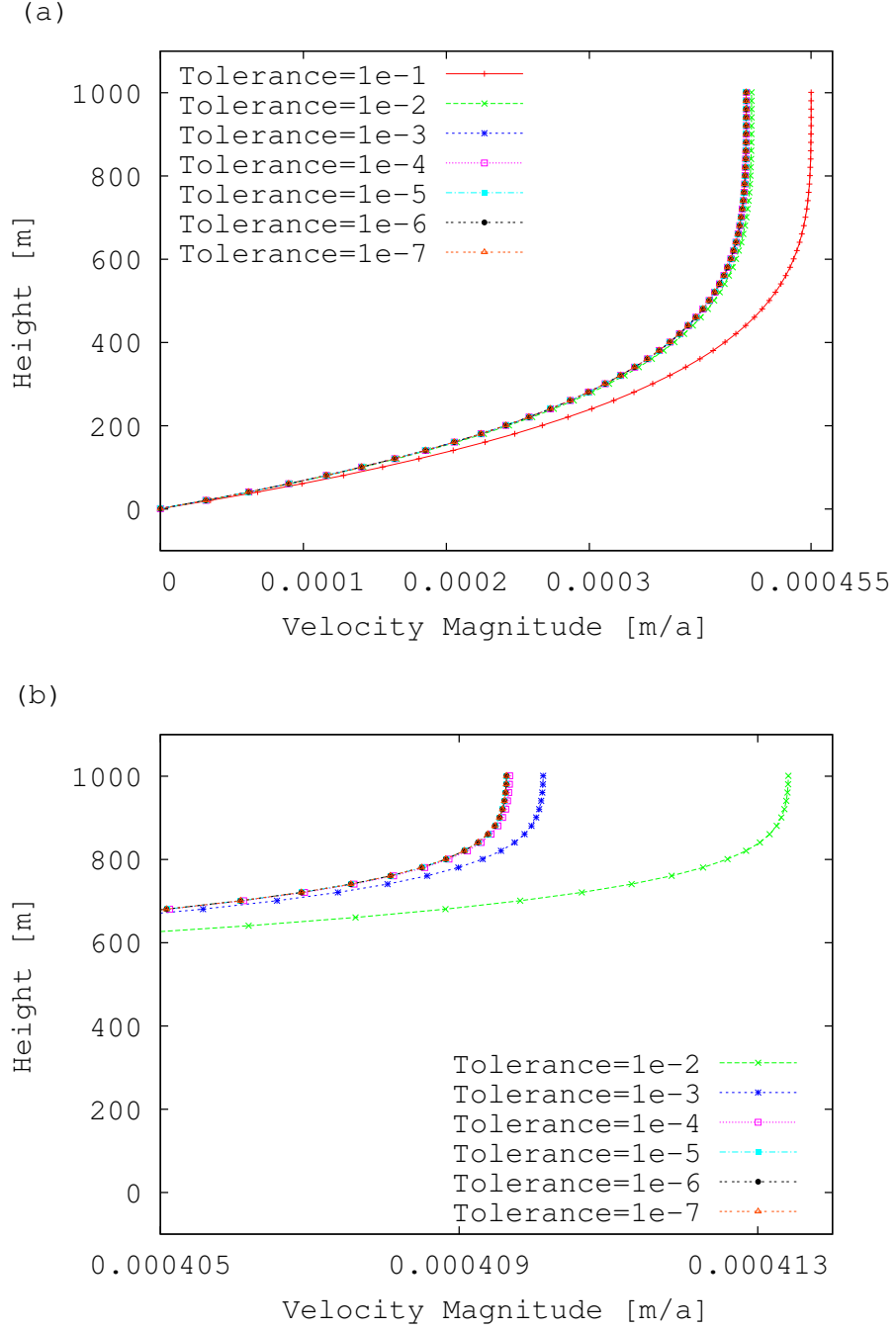


Figure 4.6: Testing the tolerance level. The number of elements is held constant at 2500. The model is run with the domain given in equation (4.1) using experiment setup A. Each run uses the convergence test in equation (3.36). The convergence acceleration parameter is 0.0. (a) the velocity magnitude profile at $x = 500$ m for runs at different tolerance levels, (b) horizontal scale adjusted to show the differences in velocity magnitude for the different tolerances tested.

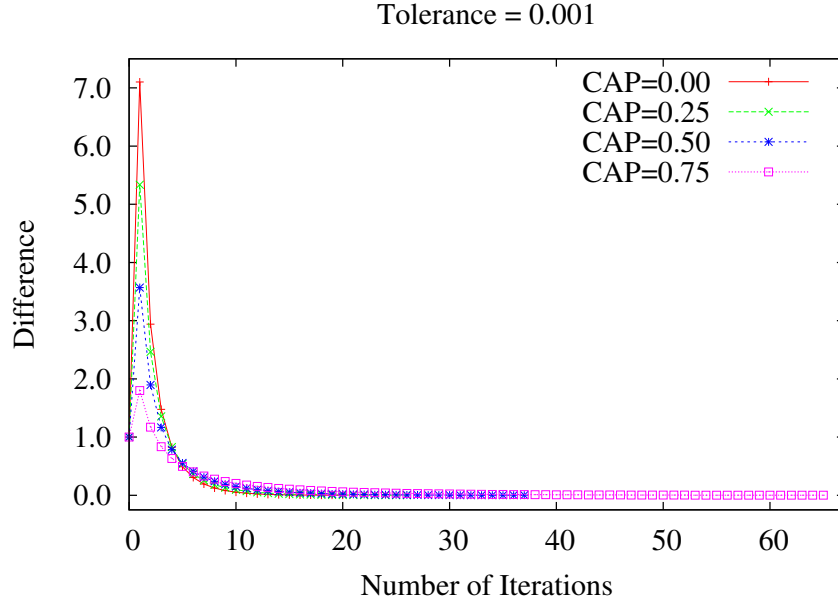
Table 4.6 shows the convergence acceleration parameter and the number of steps taken for the system to converge. The table shows a convergence acceleration parameter of zero converges in the least amount of iterations, taking only 21. The convergence acceleration parameter of 0.75 takes the longest to converge, taking 66 iterations. This is not unexpected as only 25% of the new solution is accepted at each iteration.

Convergence Acceleration Parameter	Number of steps to converge
0.0	21
0.25	27
0.50	38
0.75	66

Table 4.6: List of convergence acceleration parameters and the number of steps taken to converge. The model is run with the domain given in equation (4.1) using experiment setup A, given in Table 4.1. The tolerance is $1e - 3$. The number of elements is 2500. The aspect ratio is 1 for each test.

Figure 4.7 shows difference between consecutive runs calculated using the convergence test given in equation (3.36) as a function of the number of iterations taken to converge. The curves corresponds to the convergence acceleration parameters listed in Table 4.6. The figure shows convergence is monotonic from the second iteration until convergence is reached. Figure 4.7 also shows that a convergence acceleration parameter of 0.0 converges faster than all of the other tested values.

(a)



(b)

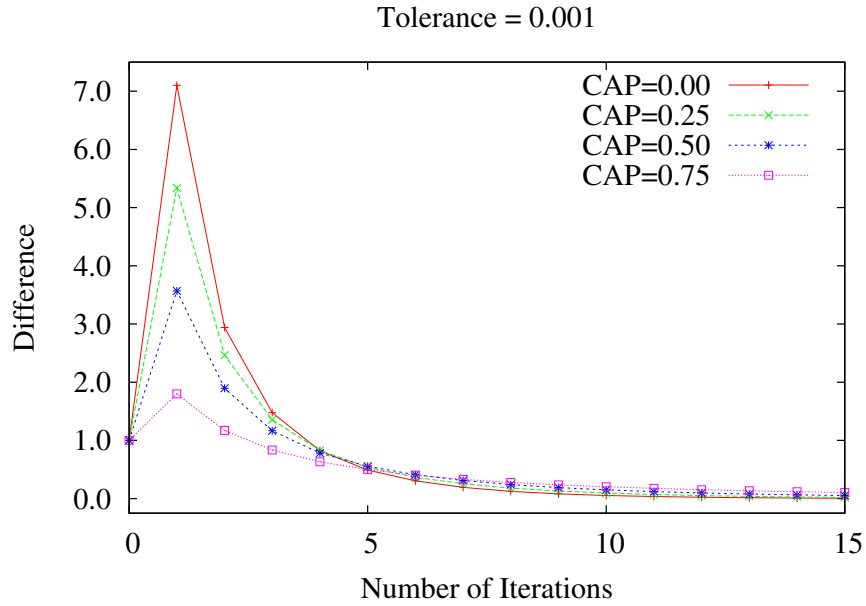


Figure 4.7: Testing the tolerance level. The number of elements is held constant at 2500 and the aspect ratio is 1. The model is run with the domain given in equation (4.1) using experiment setup A. Each run uses the convergence test in equation (3.36). The tolerance is 0.001. (a) the convergence test difference as a function of the number of iterations, (b) horizontal scale shows the first 15 iterations only.

The sensitivity tests show that the number of elements, the aspect ratio, and the tolerance level all affect the solution to which the system converges. For the system tested, too few elements can underestimate the solution and less precise tolerances overestimate the solution. The solution is also overestimated if the aspect ratio is too large. Hence, the number of elements, aspect ratio, tolerance must be considered in any application of the model to a real world ice stream. For the system tested, the convergence acceleration parameter with nonzero values took more iterations than with a convergence acceleration parameter of zero.

4.1.3 Elliptical Domain

The shallow ice approximation neglects all stress except basal stress. From [34]

$$u(h) = \frac{1}{2} \left(\frac{\rho g \alpha}{B} \right)^3 h^4 \quad (4.2)$$

where $u(h)$ is the x -component of velocity as a function of height, ρ is the density of ice, g is the acceleration due to gravity, α is the surface slope, B is a measure of ice viscosity, and h is the height of the ice at some point x . Ice is frozen to the bed in this solution, so $u(0) = 0$

The shallow ice approximation predicts an elliptical profile for an ice sheet. Consider an elliptical profile with equation

$$\frac{x^2}{50,000^2} + \frac{y^2}{1000^2} = 1 \quad (4.3)$$

with first derivative

$$\frac{dy}{dx} = \frac{-0.0004x}{\sqrt{1000^2 \left(1 - \frac{x^2}{50,000^2} \right)}} \quad (4.4)$$

The surface slope, α is found by evaluating equation (4.4) at the desired location.

Table 4.7 lists the values substituted into equation (4.2) to find the surface velocity.

Variable	Value	Units
ρ	917	kg m^{-3}
g	9.8×10^{-5}	$\text{bar m}^2 \text{kg}^{-1}$
α	0.015	
$B(T=-25\text{ }^{\circ}\text{C})$	7.207	$\text{bar} \cdot \text{a}^{1/3}$
h	800	m

Table 4.7: List of values used to calculate the surface velocity of an ice sheet with an elliptical profile.

The model is run with experiment setup A, see Table 4.1. For each run, the system runs until reaching equilibrium using the convergence test given in equation (3.36). The convergence acceleration parameter is set to 0.0. The effects of the number of elements, aspect ratio, and tolerance are also investigated. Note, the model requires ends since there is a uniform number of elements per column.

Table 4.8 lists parameter settings and results from model runs. Increasing the number of elements also increases the aspect ratio because the domain is elliptical. The table shows the solution is overestimated as the number of elements is decreased. The effect of number of elements outweighs the aspect ratio effect because the results approach a value monotonically as the number of elements increases in comparing at the same tolerance. The table also shows that the solution does not change for tolerances of $1e-6$ and $1e-7$. Hence, runs with greater numbers of elements are run only once at a tolerance of $1e-6$.

Number of elements	Average aspect ratio	Tolerance	$u(800 \text{ m}) [\text{m a}^{-1}]$
720	2.489	$1e - 3$	1.3870
		$1e - 4$	1.3854
		$1e - 5$	1.3854
		$1e - 6$	1.3851
		$1e - 7$	1.3851
1620	5.600	$1e - 3$	1.3518
		$1e - 4$	1.3502
		$1e - 5$	1.3499
		$1e - 6$	1.3499
		$1e - 7$	1.3499
3420	11.821	$1e - 3$	1.3450
		$1e - 4$	1.3433
		$1e - 5$	1.3431
		$1e - 6$	1.3431
		$1e - 7$	1.3431
5220	18.043	$1e - 3$	1.3439
		$1e - 4$	1.3422
		$1e - 5$	1.3420
		$1e - 6$	1.3420
		$1e - 7$	1.3420
7020	24.265	$1e - 6$	1.3416
		$1e - 7$	1.3416
10,620	29.5	$1e - 6$	1.3414
13,320	46.041	$1e - 6$	1.3413
17,820	61.596	$1e - 6$	1.3413
32,400	111.992	$1e - 6$	1.3412

Table 4.8: Results from model runs for comparison with the shallow ice approximation. Different mesh resolutions are tested at different tolerances. Monotonic convergence at a tolerance of $1e - 6$ shows mesh resolution dominates aspect ratio effects.

Figure 4.8 shows the velocity magnitude for the elliptical domain given by equation (4.3). The model computes $u = 1.3412 \text{ m a}^{-1}$ at $x = 30,000 \text{ m}$ and $y = 800 \text{ m}$.

Substituting the values given in Table 4.7 into equation (4.2) yields a surface velocity, $u(800 \text{ m}) = 1.3400 \text{ m a}^{-1}$ at $x = 30,000 \text{ m}$. The difference is thus 0.09%. Exact agreement is not expected because the model neglects no stresses but the shallow ice approximation neglects all stresses except basal drag. In particular, the model includes longitudinal deviatoric stresses, σ'_{xx} . The model finds the deviatoric shear stress is 1.059 bars at the bed compared to the longitudinal deviatoric stress which is 0.000608 bars at the bed. Thus deviatoric shear stress is the dominant stress. However the longitudinal stress is a percentage of the deviatoric stress and thus the difference in velocities is different by a percentage.

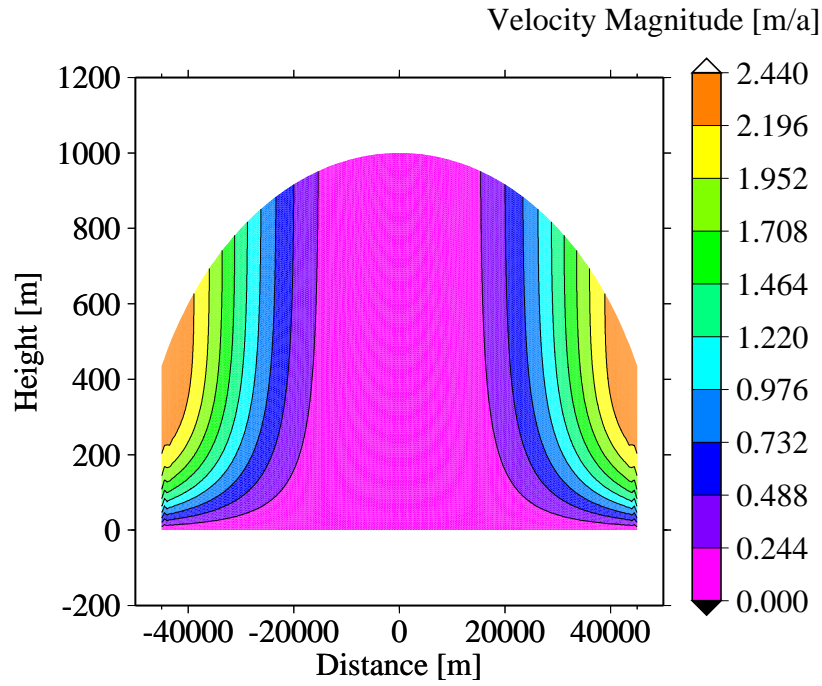


Figure 4.8: Elliptical domain, velocity field. The model is run with experiment setup A, see Table 4.1. The system is tested for convergence using the test given in equation (3.36) with a tolerance of $1e-6$ and 32,400 elements. The run corresponds to the last run given in Table 4.8.

4.1.4 Uniform Slab of Floating Ice

The next test compares model output with Weertman thinning of a uniform slab of floating ice. Thus the basal traction is negligible. Consider an isothermal uniform slab with thickness, H , floating in water. Let y be positive up. Let the length be 200 km in the x -direction, and 1000 m in the y -direction. The model uses experiment setup B, see Table 4.2. The system runs until equilibrium is reached using the convergence test given in equation (3.36) with a tolerance of $1e-4$. There are 8,000 elements and the average aspect ratio is 2.5.

From [44]

$$\dot{\epsilon}_{xx} = \left(\frac{\rho_I g H}{4B} \left(1 - \frac{\rho_I}{\rho_W} \right) \right)^3 \quad (4.5)$$

where ρ_I is the density of ice, ρ_W is the density of sea water, g is the gravitational constant, and B is a viscosity measure of the ice. The first assumption is that the length of the slab is many orders of magnitude greater than the thickness, H . The second assumption is that equation (4.5) is valid far from the edge [44].

Also,

$$\dot{\epsilon}_{xx} + \dot{\epsilon}_{yy} = 0 \quad (4.6)$$

because thinning in the vertical results in the stretching in the horizontal.

Table 4.9 lists the values substituted into equation (4.5) to find $\dot{\epsilon}_{xx}$. Equation (4.6) then gives the thinning rate, $\dot{\epsilon}_{yy}H = 199.73 \text{ m a}^{-1}$.

Figure 4.9 shows that the strain rate is nearly uniform over the block of ice except where it is thinning on the ends due to an imbalance of forces there. The model calculates a value of $\dot{\epsilon}_{yy} = -0.1998 \text{ a}^{-1}$. Multiplying this by the ice height yields a thinning rate of 199.8 m a^{-1} . The difference between the model and the Weertman thinning approximation is 0.035%.

Variable	Value	Units
ρ_I	917	kg m ⁻³
ρ_W	1028	kg m ⁻³
g	9.8×10^{-5}	bar m ² kg ⁻¹
H	1000	m
B(T=-10 °C)	4.15	bar · a ^{1/3}

Table 4.9: List of values used to calculate the Weertman thinning rate of a uniform slab of ice.

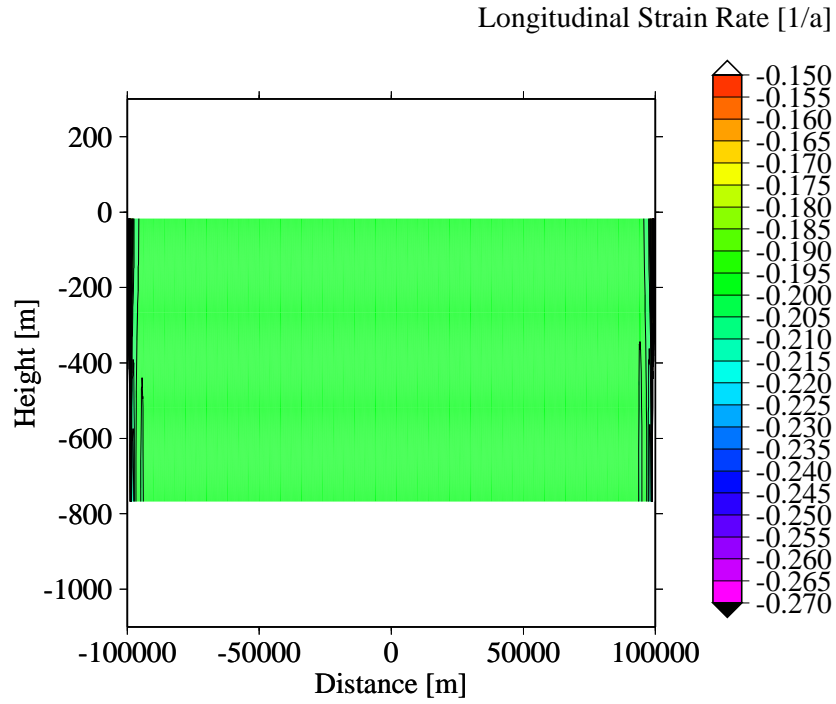


Figure 4.9: Uniform slab, strain rate. The model is run with experiment setup B, see Table 4.2. The system runs until equilibrium is reached using the convergence test given by equation (3.36) with a tolerance of $1e - 4$. The Weertman thinning rate is 199.8 m a^{-1} , found by multiplying strain rate by height, $\dot{\epsilon}_{yy}H$.

Figure 4.10 shows results from a second run for model comparison with Weertman thinning. The figure shows a plot of the difference between consecutive runs calculated using the convergence test given in equation (3.36) as a function of the number of iterations taken to converge. The model is run with experiment setup B, see Table 4.2. The system uses the convergence test given in equation (3.36) with a tolerance of $1e - 6$. The system did not reach equilibrium in 20,000 iterations. In comparison, the model converged in 43 steps using a tolerance of $1e - 5$.

4.1.5 Thermodynamic Studies

In the thermodynamic sensitivity studies, the first configuration tested consists of a rectangular steady-state slab of ice. The first test checks that the temperature solver can calculate interior temperatures given the boundary temperatures. The model runs with the velocity boundary conditions given in experiment setup A, see Table 4.1. I impose isothermal boundaries of $T = -30\text{ }^{\circ}\text{C}$ everywhere on the boundaries and do not impose any temperatures in the interior. The velocity of the system is zero because there is no imbalance of force applied at the sides and the surface slope is zero. The system uses the temperature convergence test described in section 3.8.2.

Figure 4.11 shows the uniform temperature field calculated by the model. The model yields the exact result of $T = -30\text{ }^{\circ}\text{C}$ everywhere in the interior of the problem domain.

The second test checks that the temperature solver can calculate temperatures given a surface temperature and a heat flux at the bed. The problem domain consists of the rectangular steady-state slab of ice. The model runs with the velocity boundary conditions given in experiment setup A, given in Table 4.1. The specified surface temperature is $-36.5\text{ }^{\circ}\text{C}$ and a geothermal flux of $3.17 \times 10^5\text{ cal a}^{-1}\text{ m}^{-2}$, equivalent to 42 mW m^{-2} is specified at the bed. The sides have implied zero flux

boundary conditions because there are no explicit conditions specified. As in the previous test, the velocity of the system is zero because there is no imbalance of force applied at the sides and the surface slope is zero. Hence both advection and internal heating are negligible. The system uses the convergence test described in section 3.8.2.

Figure 4.12 shows the test which yields excellent results with a maximum difference between the program solution and the exact result of 1.55%. The difference is due to the thermal conductivity and specific heat. The exact result uses constant thermal conductivity and specific heat, whereas the model uses temperature dependent calculations for both parameters. The figure shows that conduction dominates and temperature decreases linearly with depth.

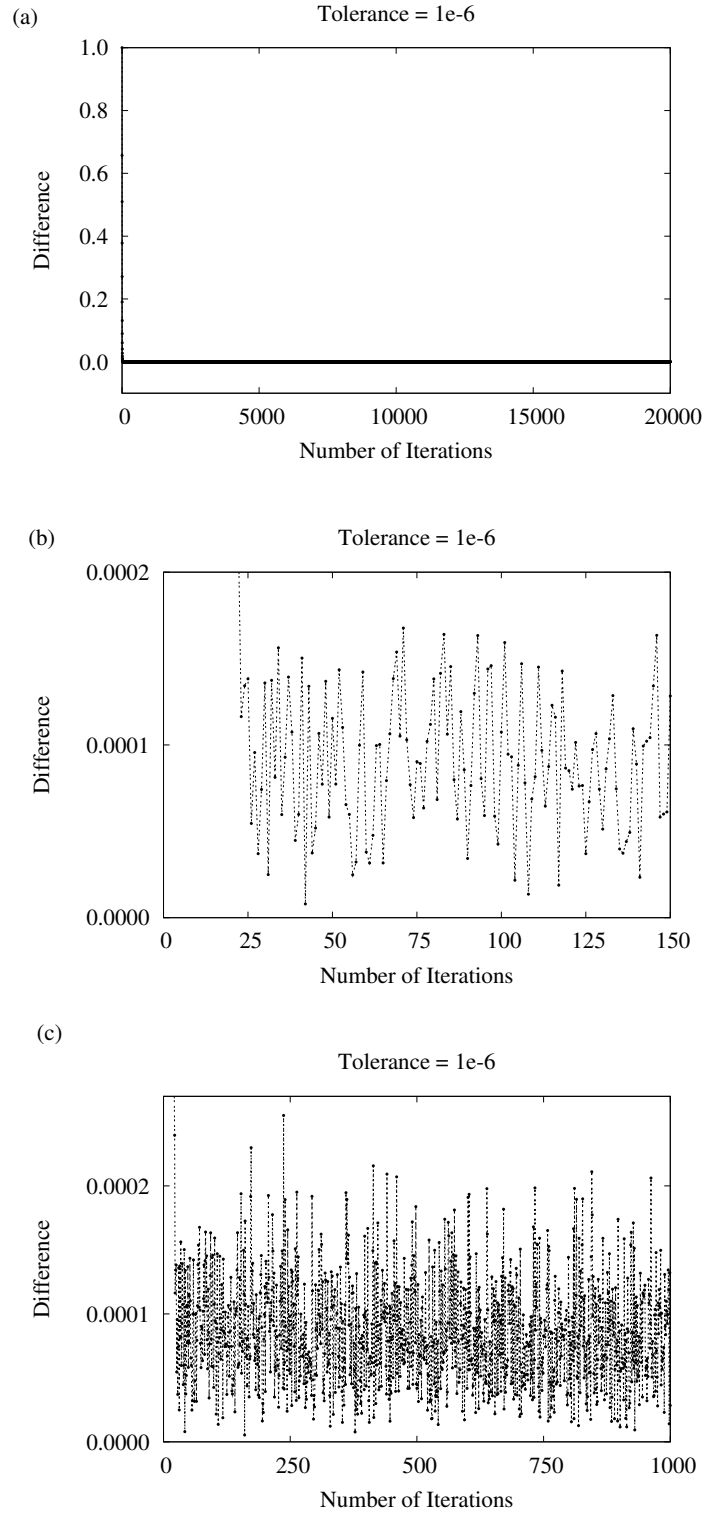


Figure 4.10: Second run for comparison with Weertman thinning. The model is run with experiment setup B, see Table 4.2. The system did not reach equilibrium in 20,000 iterations. (a) 20,000 iterations, (b) the first 100 iterations, (c) the first 1000 iterations

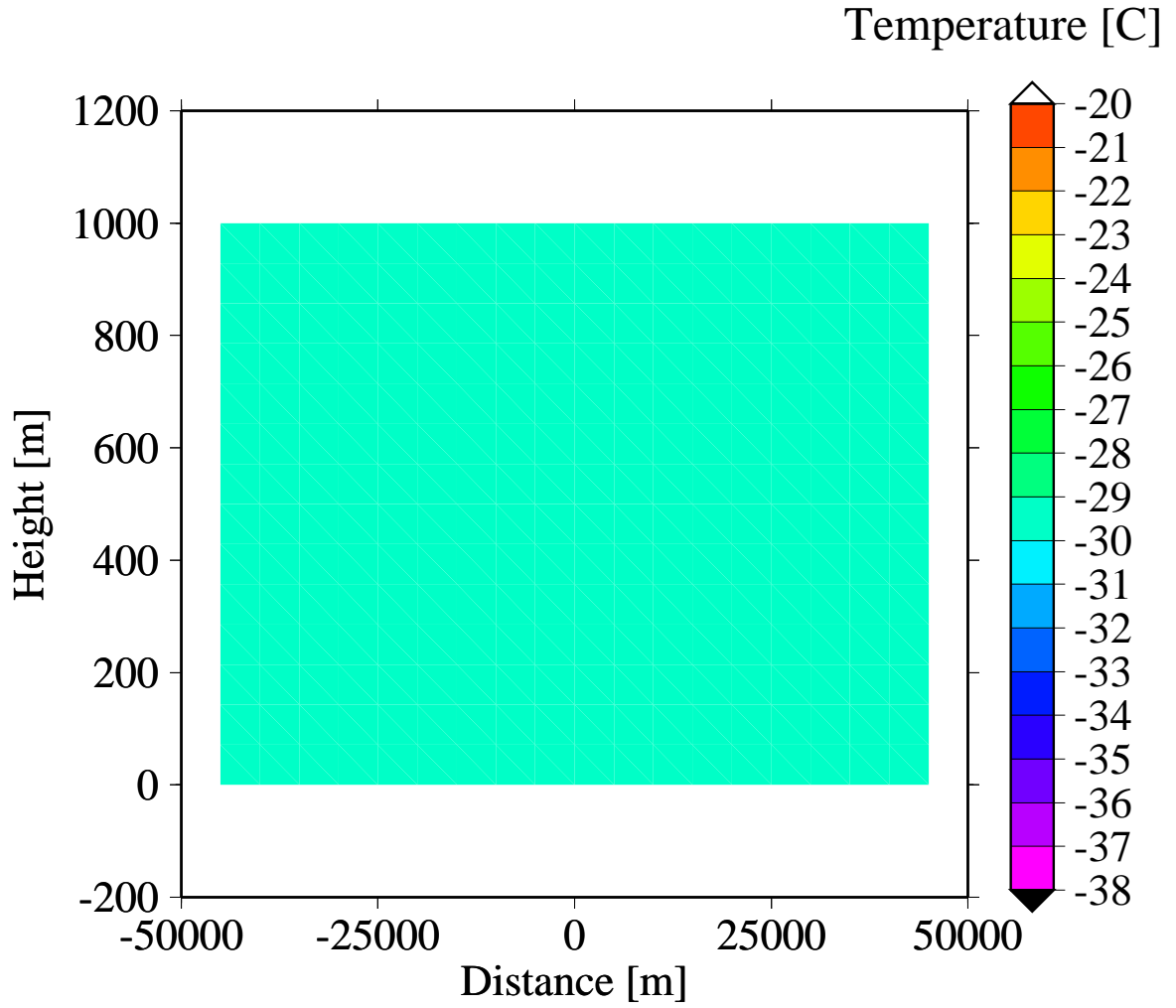


Figure 4.11: Thermodynamic test with a steady-state slab of ice, isothermal boundaries. The model is run with velocity boundary conditions given in experiment setup A, see Table 4.1. The temperature boundaries are isothermal. The system uses the convergence test described in section 3.8.2. The model calculates the uniform temperature field in the interior of the problem domain.

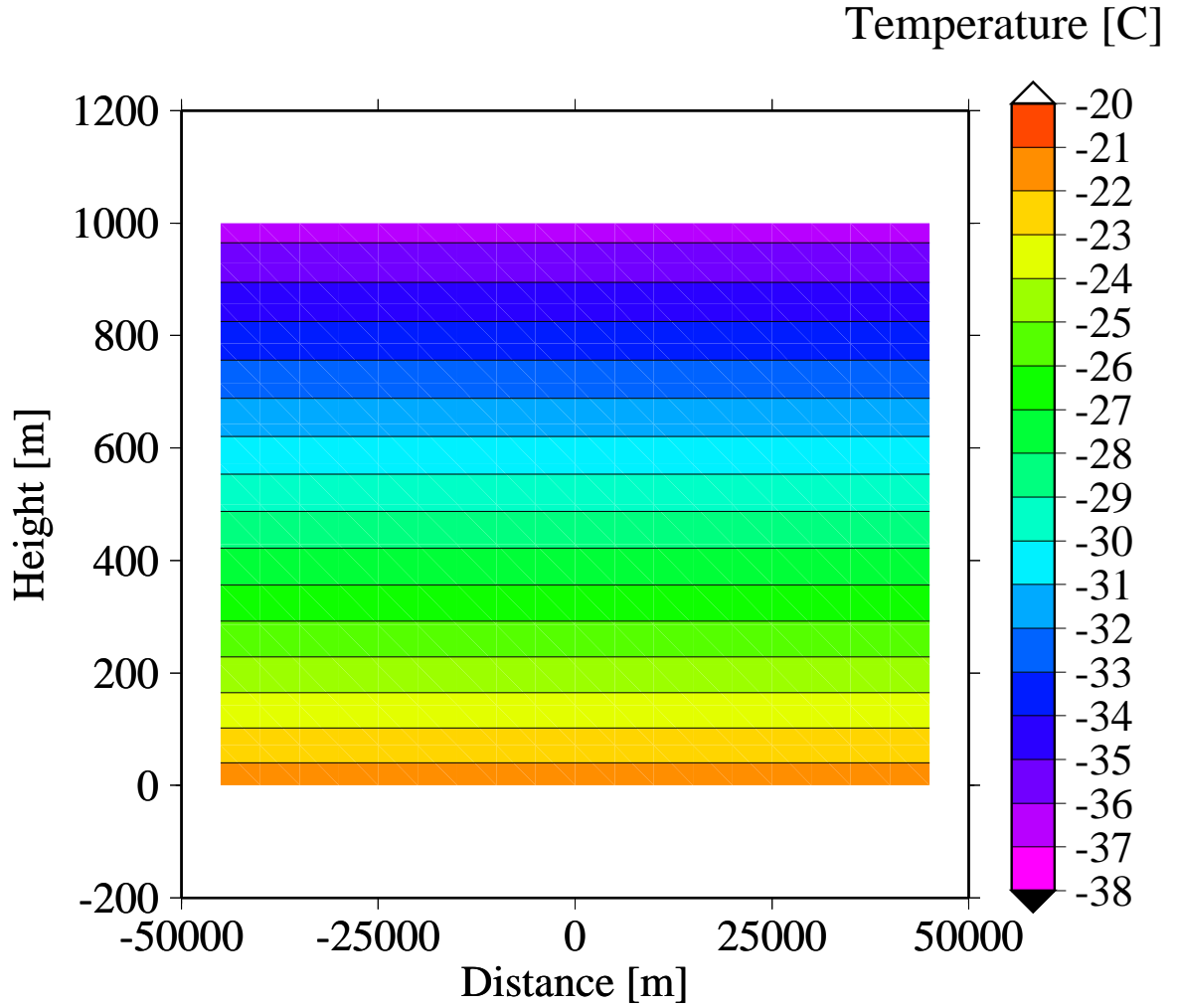


Figure 4.12: Thermodynamic test with a steady-state slab of ice, advection. The model runs with velocity boundary conditions given in experiment setup A, see Table 4.1. The system uses the convergence test described in section 3.8.2. The surface temperature is specified and geothermal flux is specified at the bed. Zero velocity results in the solution dominated by conduction with temperature decreasing linearly with depth.

The final test of the temperature solver checks advection with strain heating. The model runs with the velocity boundary conditions given in experiment setup A, given in Table 4.1. The right end of the problem domain has more height than the left end of the problem domain, hence velocity is nonzero. The surface temperature is specified as discussed in section 4.1.1. Geothermal flux of $3.17 \times 10^5 \text{ cal a}^{-1} \text{ m}^{-2}$, equivalent to 42 mW m^{-2} is applied at the bed. The basal slippery layer is present with a thickness of 10 m. The system uses the convergence described in section 3.8.2.

Figure 4.13 shows the cold surface temperatures are advected downstream in the direction of flow. In the first 100 km, temperature gets colder with depth before warming near the bed. Horizontal advection causes this temperature inversion. Vertical advection causes the cold ice to move toward the bed.

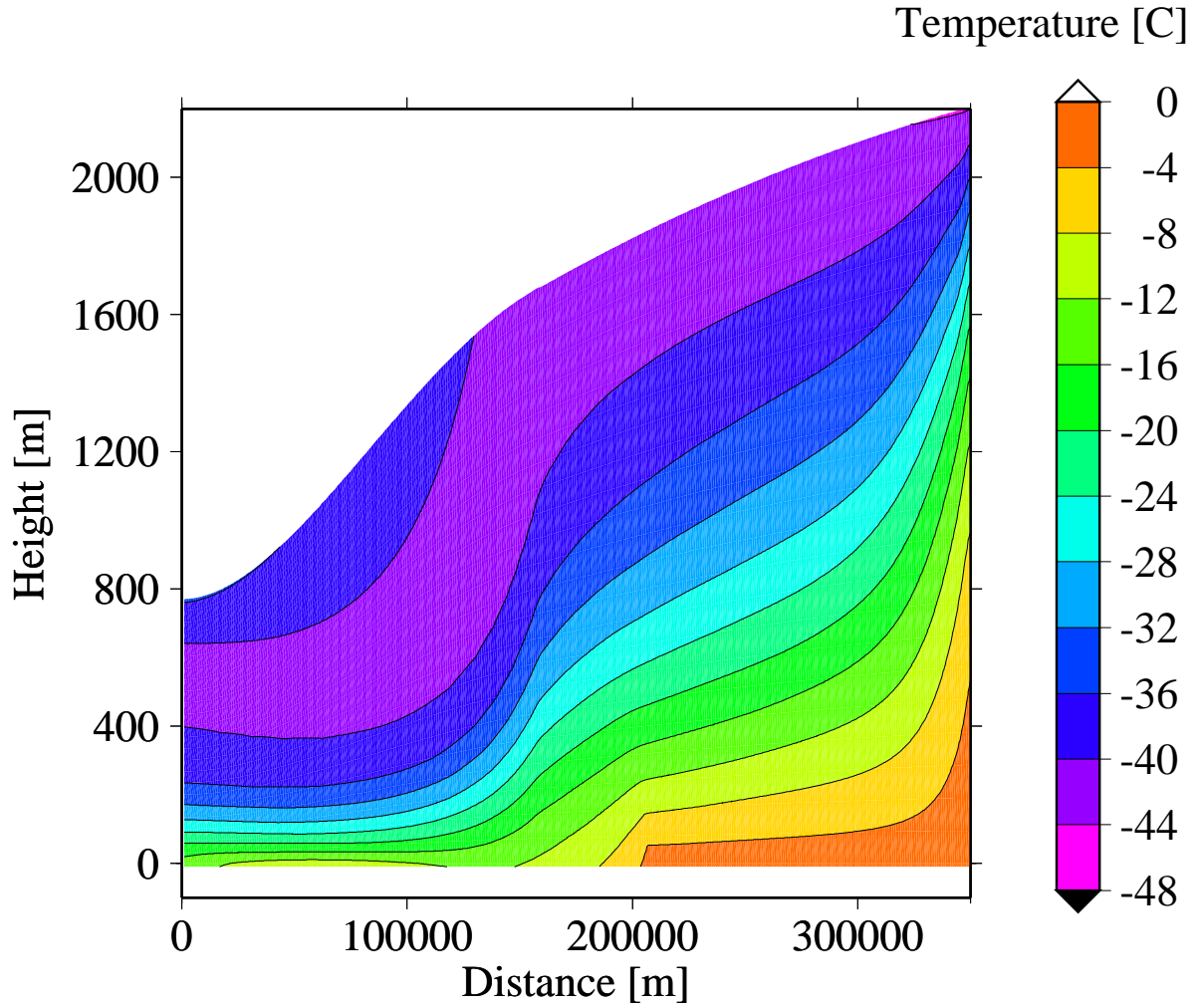


Figure 4.13: Advection thermodynamic test. The model runs with velocity boundary conditions given in experiment setup A, see Table 4.1. Surface temperatures are set as described in section 4.1.1 and geothermal flux of $3.17 \times 10^5 \text{ cal a}^{-1} \text{ m}^{-2}$, equivalent to 42 mW m^{-2} is specified at the bed. The system uses the convergence test described in section 3.8.2. Cold ice is advected downstream.

Figure 4.14 shows the surface of the domain and the temperature profile taken at $x = 75,000$ m. The figure shows the temperature inversion due to cold ice being advected downstream.

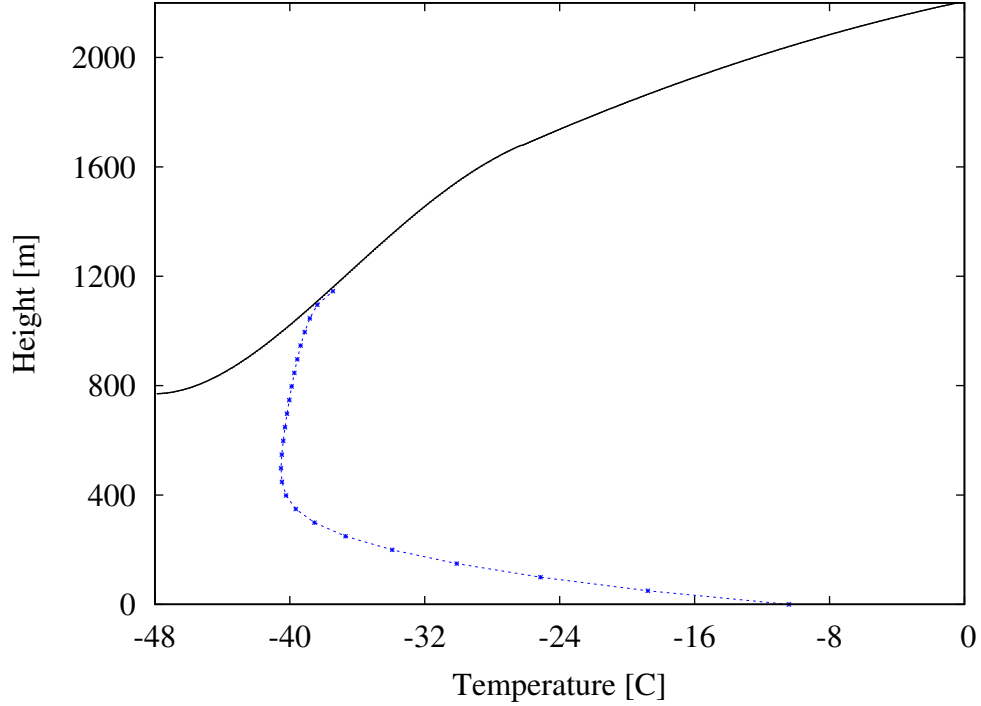


Figure 4.14: Advection thermodynamic test, temperature profile. The model runs with velocity boundary conditions given in experiment setup A, see Table 4.1. Surface temperatures are set as described in section 4.1.1 and geothermal flux of $3.17 \times 10^5 \text{ cal a}^{-1} \text{ m}^{-2}$, equivalent to 42 mW m^{-2} is specified at the bed. The system uses the convergence test described in section 3.8.2. The temperature inversion is due to cold ice being advected downstream.

4.2 Whillans Ice Stream

The results of modeling Whillans Ice Stream are presented in this section. The model runs use experiment setup C given in Table 4.3. Each run has a mesh resolution with 16,896 elements. The basal slippery layer is present with a thickness of 10 m. For each test the system run until equilibrium is reached using the convergence test given in equation (3.36). The tolerance is $1e - 5$.

The profile starts at the grounding line and extends inland. The model does not include ice shelf behavior. Thus, supporting the left hand side with water makes it a calving front. Hughes, (for example, see [21]), has also used this simplification.

The test runs described previously in section 4.1.2 show that aspect ratio can affect the solution. However, test runs previously described in section 4.1.3 show that the mesh resolution can dominate aspect ratio effects. Thus each system must be checked for aspect ratio effects. Aspect ratio is defined as the ratio of width to height. This presents a problem for modeling ice sheets since the lateral extent of interest is generally several hundreds of kilometers whereas the vertical height is only a few thousand meters. In the finite element mesh, columns are added by linear interpolation to minimize the effects of aspect ratio. Figure 4.15 (a) shows the node configuration for all of the Whillans Ice Stream runs. There is a uniform number of rows per column. Figure 4.15 (b) shows the first 50 km to show the node spacing. The number of columns is determined by input data and interpolation.

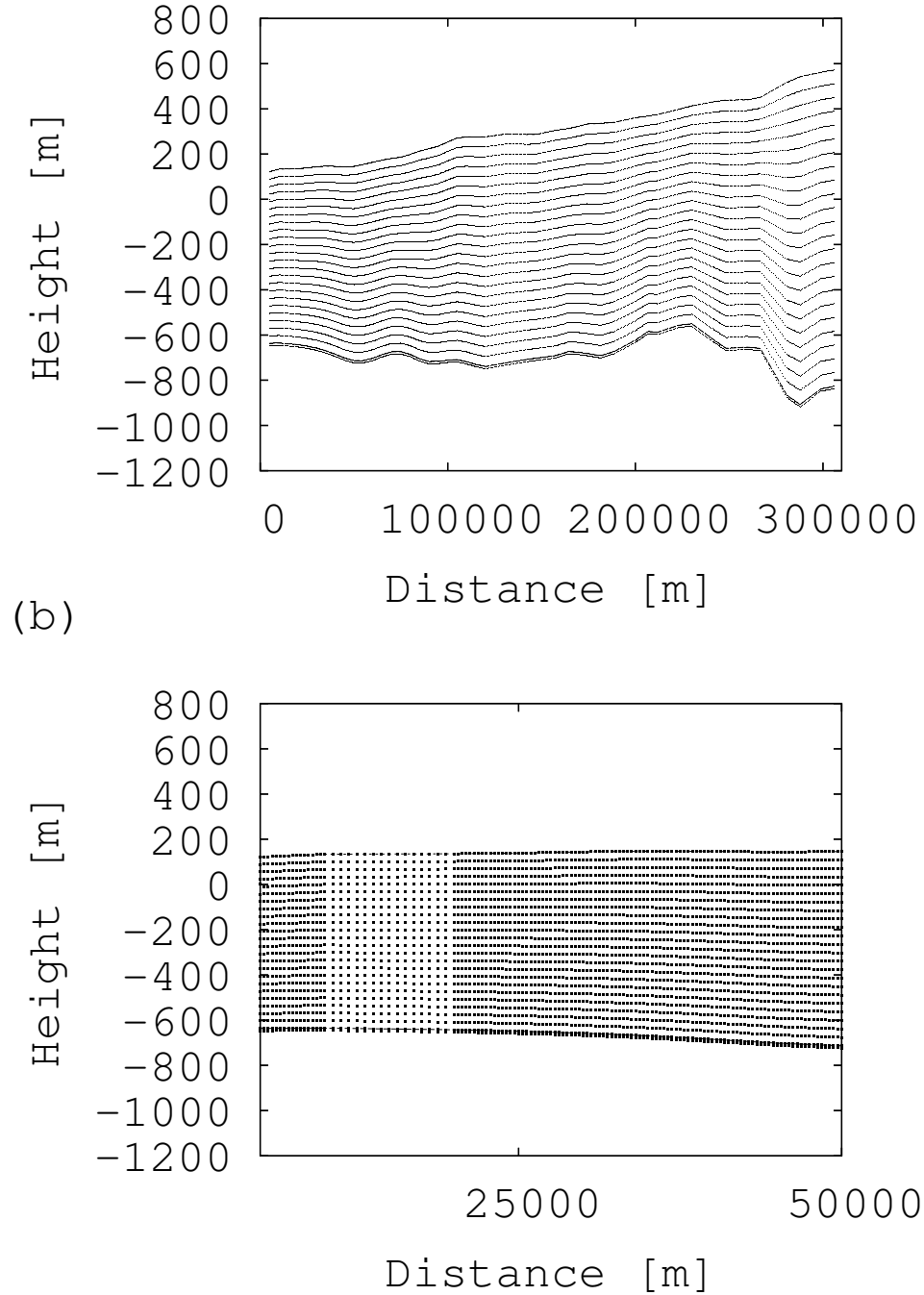


Figure 4.15: Plot of node configuration for Whillans Ice Stream with the basal slippery layer. (a) the entire problem domain and (b) the first 50 km. Vertical columns are determined by input data and interpolation. Aspect ratio is minimized by interpolation and setting horizontal rows accordingly.

Figure 4.16 shows the aspect ratio is 20 or less in the interior and near 90 in the basal slippery layer.

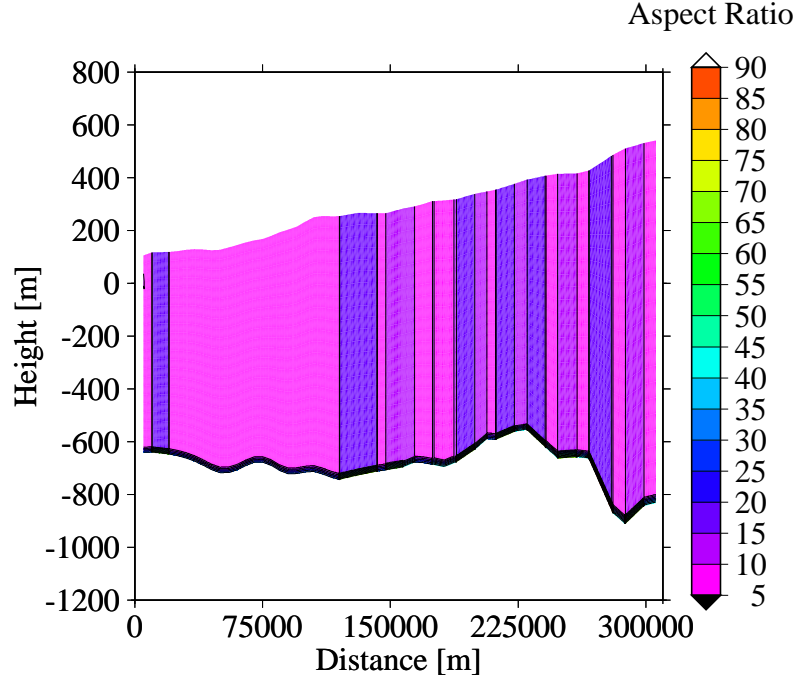


Figure 4.16: Plot of aspect ratio for Whillans Ice Stream with the basal slippery layer. The model is run with experiment setup C. The aspect ratio is 20 or less in the interior and near 90 in the basal slippery layer.

Figure 4.17 (a) which includes the basal slippery layer shows that the x -component of the velocity is greatest near the grounding line and in the first 100 km of the profile. The large velocity at the grounding line is due to the calving front. Plug flow dominates in the interior. Figure (b) which has no slippery layer shows that the x -component of the velocity for the system is also greatest near the grounding line. The system with no slippery layer, has velocities slower by an order of magnitude. Both figures are scaled to show interior velocities.

Figure 4.18 shows that the x -component of velocity is nearly plug flow. The variation in velocity from the surface to the bed is 2 m a^{-1} . The profile is taken from Figure 4.17 at $x = 35,000 \text{ m}$.

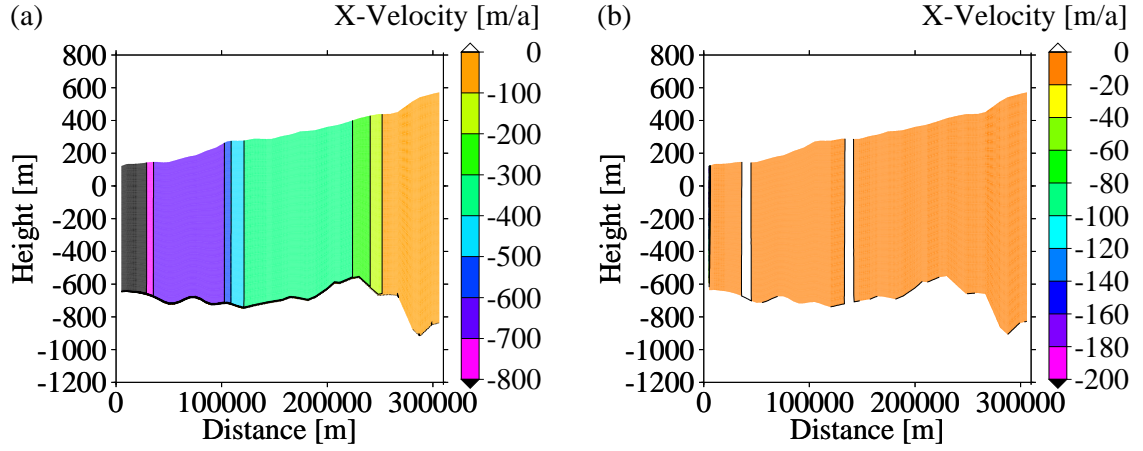


Figure 4.17: Plot of x -component of velocity for Whillans Ice Stream. The model is run with experiment setup C. (a) with the basal slippery layer and (b) with no basal slippery layer. Note the calving front is off the scale in order to show the velocities in the interior.

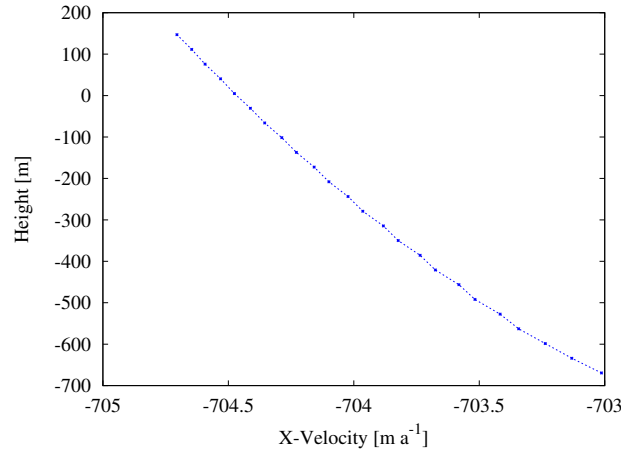


Figure 4.18: Profile plot of x -component of velocity for Whillans Ice Stream. The model is run with experiment setup C. The profile is taken from Figure 4.17 at $x = 35,000$ m.

The y -component of the velocity including the basal slippery layer, Figure 4.19 (a), is downward except in areas where the bed has negative slope. Thus u_y is upward where ice moves upslope. Thinning occurs near 225 km as surface velocities are downward and velocities near the bed are upward. Thinning may also occur where downward surface velocities are higher than downward basal velocities. The figure shows large downward velocities at the grounding line consistent with a calving

front. Figure 4.19 (b) shows that with the exception of the the left end, the velocities are the same order of magnitude for the system with no basal slippery layer.

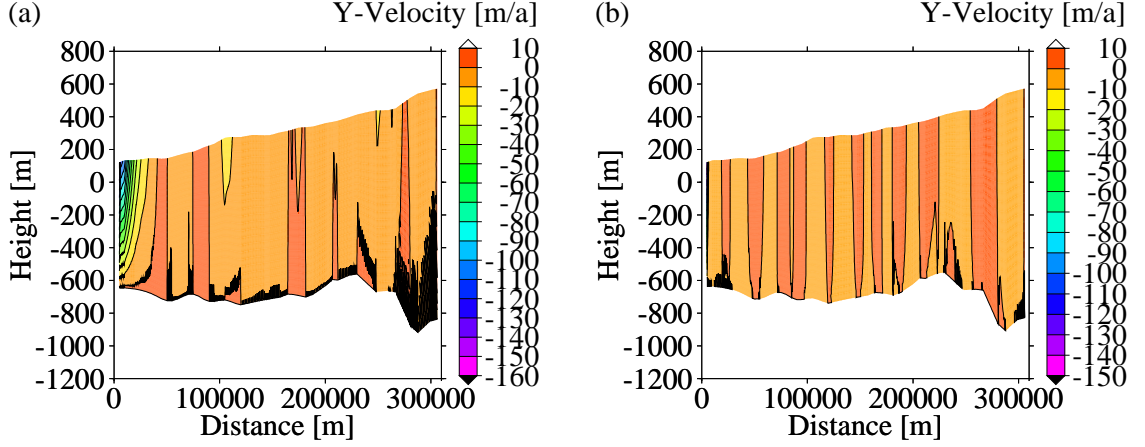


Figure 4.19: Plot of y -component of velocity for Whillans Ice Stream. The model is run with experiment setup C. (a) with the basal slippery layer and (b) with no basal slippery layer. For the system with the basal slippery layer, the large downward velocities are consistent with a calving front.

Figure 4.20 (a) shows that, with the basal slippery layer, the largest velocity is in the first 25 km. This is consistent with a calving front. Since the x -component of the velocity is much larger compared to the y -component of velocity as seen in Figures 4.17 and 4.19, the velocity magnitude shows plug flow in the interior of the ice stream. Figure 4.20 (b) shows that with no basal slippery layer the velocities are largest in the front but are much lower in the interior compared to the system with the basal slippery layer.

Figure 4.21 shows that the horizontal strain rate for Whillans Ice Stream is extending with larger values when the basal slippery layer is present compared to when the basal slippery layer is not there. However, there is more compression in the system with no basal layer.

Figure 4.22 shows the vertical strain for cases with and without the basal slippery layer for Whillans Ice Stream. Both figures complement respective horizontal strain rates given in Figure 4.21.

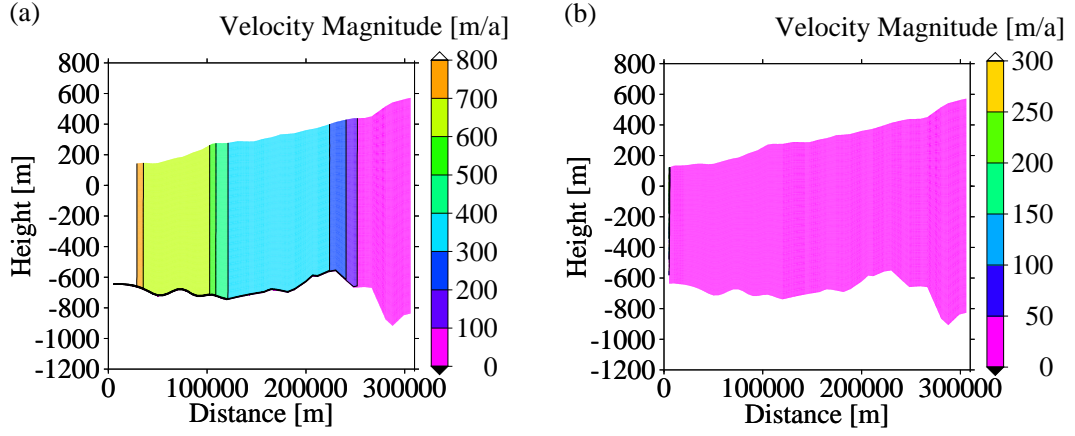


Figure 4.20: Plot of velocity magnitude for Whillans Ice Stream. The model is run with experiment setup C. (a) with the basal slippery layer and (b) with no basal slippery layer. The velocities are much faster in the system that has the basal slippery layer.

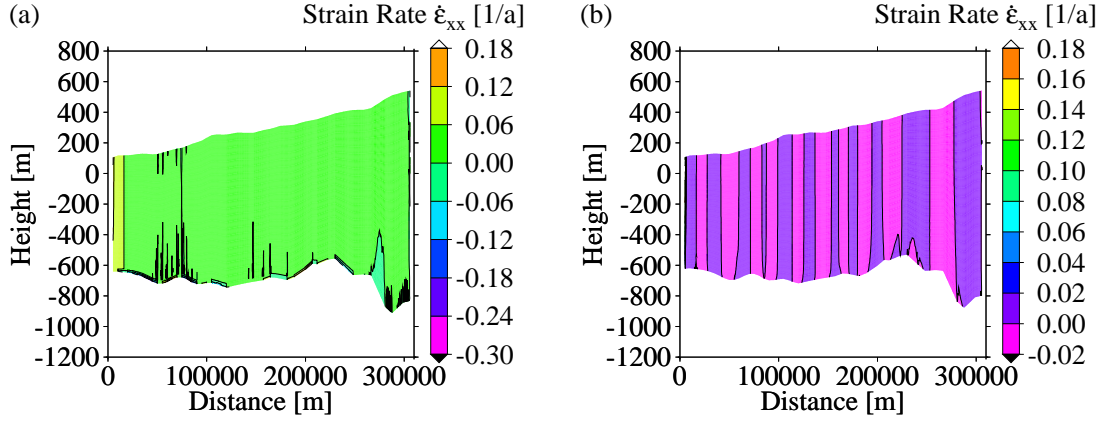


Figure 4.21: Plot of horizontal strain rate for Whillans Ice Stream. The model is run with experiment setup C. (a) with the basal slippery layer and (b) with no basal slippery layer.

The slippery layer is a parameterization of sliding much as Weertman's sliding model is. Both are based on physically plausible scenarios. A 10 m thick slippery layer thickness is negligible compared to the ice stream thickness. Rheology (softness) of the slippery layer is tuned to the ice stream being modeled.

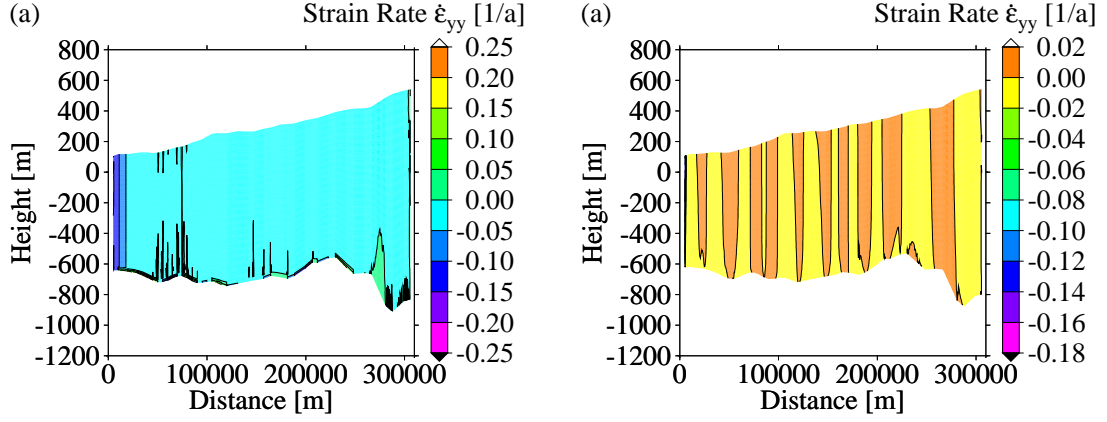


Figure 4.22: Plot of vertical strain rate for Whillans Ice Stream. The model is run with experiment setup C. (a) with the basal slippery layer and (b) with no basal slippery layer.

Figure 4.23 shows two versions of softening in the basal slippery layer: a uniform softening and a linear increase in softening with distance down flow. Traditionally, a linear increase is used, for example see Payne et al [40].

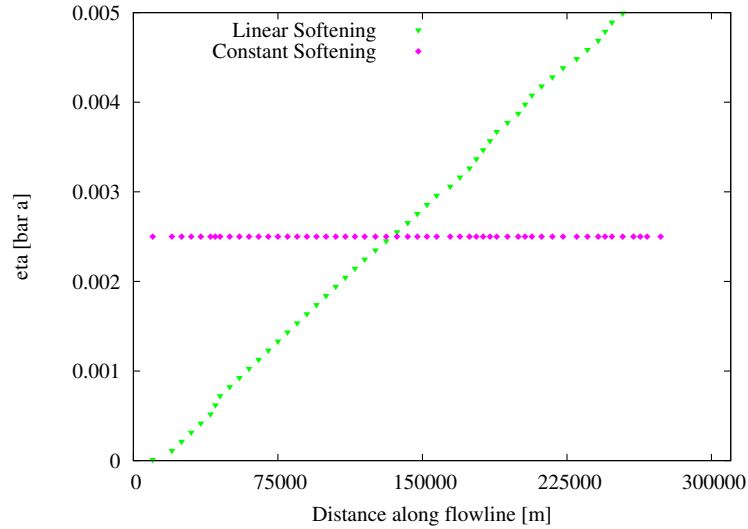


Figure 4.23: Plot of the ice hardness for Whillans Ice Stream with the basal slippery layer. The model runs with experiment setup C. The two kinds of softening tested.

In contrast, with linear softening in the basal slippery layer, Figure 4.24 (b) shows that the velocities are much larger than those shown in Figure 4.24 (a). With

both types of softening there is plug flow, however with linear softening the ice is moving much faster. In comparison, in the first 30 km, the velocities with uniform softening in the basal slippery layer are near 2600 m a^{-1} while the velocities with the linear softening in the basal layer are much faster at $15,750 \text{ m a}^{-1}$.

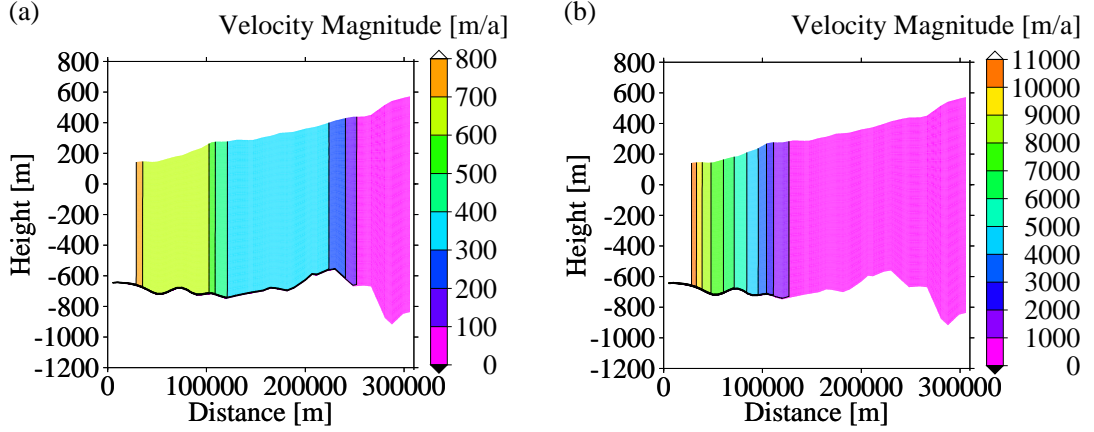


Figure 4.24: Plot of velocity magnitude for Whillans Ice Stream, comparison of softening in the basal slippery layer. The model is run with experiment setup C. (a) uniform softening of the basal slippery layer and (b) a linear increase in softening with distance down flow. Note the difference in velocity scales shows the system has faster velocities with a linear increase in softening of the basal slippery layer.

Figure 4.25 shows the surface velocity for Whillans Ice Stream using constant softening in the basal slippery layer. Shown are measured values [33, 43, 17, 29], model values, and values from an earlier non-multiphysics version of the model that does not include temperature. Velocities in the present model have a pattern similar to that in the earlier version. Comparison of the modeled values with measured ones shows that the model agrees, on average, with the measured values. There are no measured data between 130 km and 160 km.

Figure 4.26 shows the surface velocity of Whillans Ice Stream in comparison with velocities calculated using different softening patterns in the model. Velocities found using uniform softening along the profile agree better with the measured

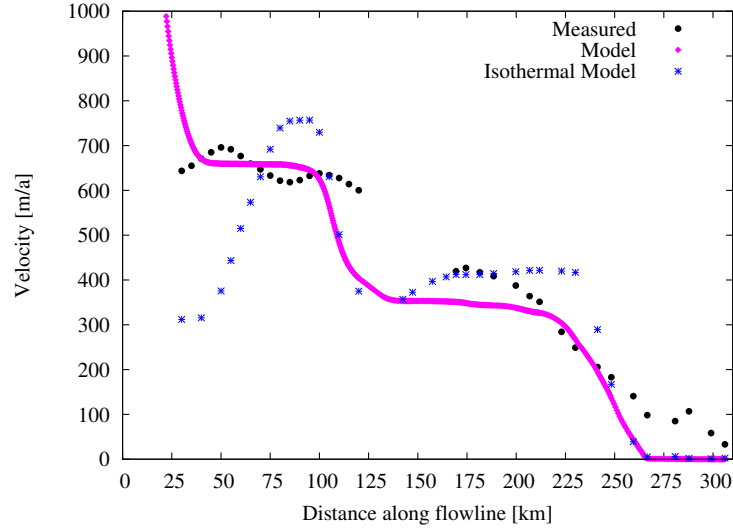


Figure 4.25: Plot of surface velocity for Whillans Ice Stream with the basal slippery layer. The model is run with experiment setup C.

surface velocities than with those calculated using a linear progression of softening.

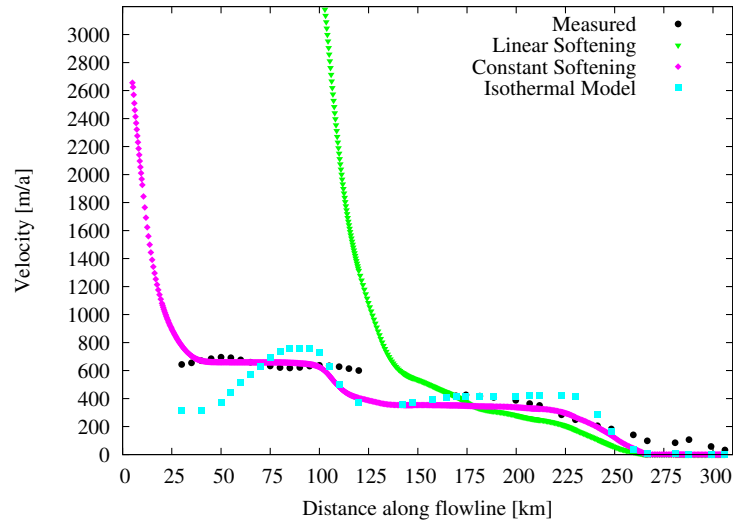


Figure 4.26: Plot of surface velocity for Whillans Ice Stream with the basal slippery layer softening comparison. The model uses experiment setup C.

As discussed in section 2.4.6, large values of the peclet number indicate regions where advection dominates conduction. The model with the basal slippery layer

shows large peclet values in much of the flowline with the largest values near the grounding line, Figure 4.27 (a) where velocities are highest, (Figure 4.17 a). For the model with no slippery layer, Figure 4.27 (b) shows the peclet number is 84 or less in the interior and is near 840 at the grounding line.

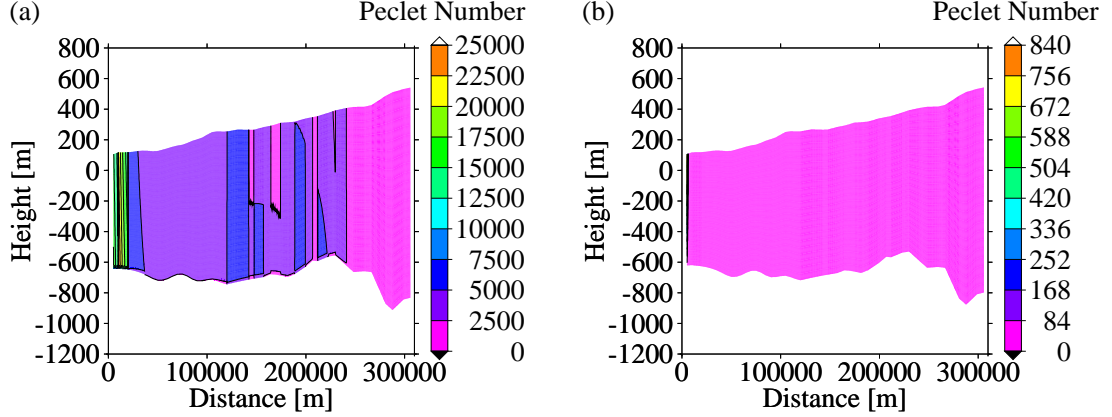


Figure 4.27: Plot of peclet for Whillans Ice Stream. The model is run with experiment setup C. (a) with the basal slippery layer and (b) with no basal slippery layer.

The effects of strain heating are found by taking the difference between runs that vary only in whether strain heating is present. Figure 4.28 shows that strain heating causes an increase in temperature at the bed by as much as 5.5°C .

As expected, either with or without the basal slippery layer, temperatures are lowest at the surface and warmest at the bed (Figure 4.29). For the system with the basal slippery layer, the interior temperatures are consistent with the peclet numbers shown in Figure 4.27 (a), the velocities given in Figure 4.17 (a), and the increase in temperature due to strain heating at the bed, as shown in Figure 4.28. Figure 4.29 also shows in the region where the basal slippery layer is not specified, from 280 km to 310 km, the temperatures are conduction-like due to vertical advection in agreement with Figure 4.19 (a). The system without the basal slippery layer shows conduction-like temperatures in agreement with velocities shown in Figures 4.17. Both systems show an upward movement of temperatures where the bed has

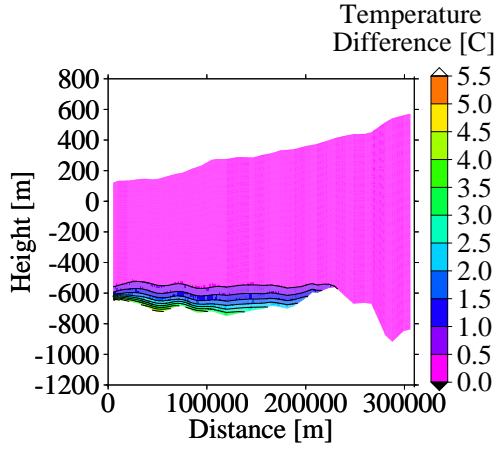


Figure 4.28: Plot of thermal effects of strain heating for Whillans Ice Stream. The model is run with experiment setup C. Taking the difference between model runs with and without strain heating shows and increase in temperature at the bed by as much as 5.5 °C.

negative slope. The side boundary conditions are difficult since they are unknown; specifying none implies a zero flux on the boundary in the model. However, on the first iteration, using the surface temperature and flux at the bed, an applied flux that varied linearly with depth is specified.

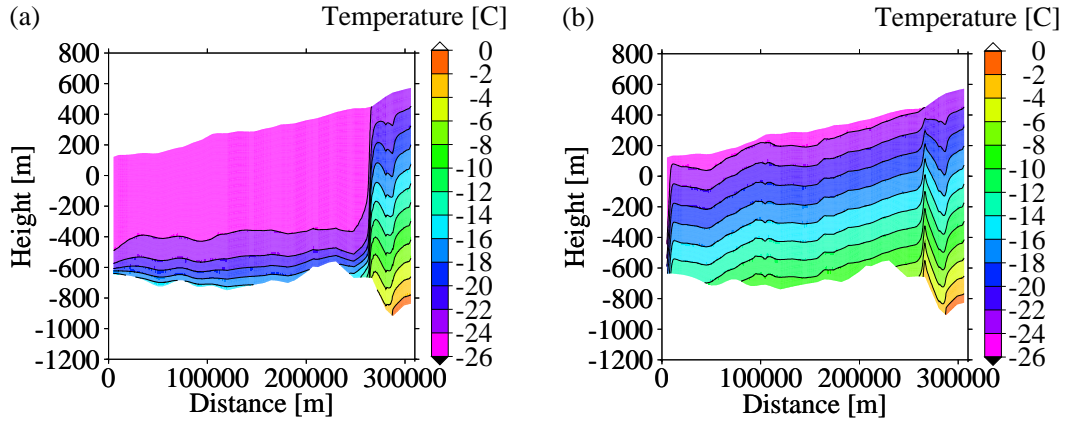


Figure 4.29: Plot of temperature for Whillans Ice Stream. The model is run with experiment setup C. (a) with the basal slippery layer and (b) with no basal slippery layer.

Chapter 5

CONCLUSIONS

This work presents an approach to modeling ice streams as a multiphysics system of coupled components. The finite element method provides the machinery for solving differential equations in such a multiphysics system that is also nonlinear due to material properties. A slippery layer approach is a parameterization of sliding. This layer deforms faster but has negligible thickness compared with the ice thickness. The softness of the slippery layer is tuned to the ice stream being modeled.

Verification studies showed mesh resolution and aspect ratio are system dependent parameters. For example in comparing surface velocities calculated from the model with surface velocities calculated analytically, the aspect ratio was dominated by mesh resolution. That is, aspect ratios greater than 100 did not affect the calculations. The convergence test computes the difference between consecutive runs and compares to a tolerance. Solutions of greater precision are reached for smaller and smaller tolerances. However, the gains in precision become smaller and smaller as the tolerance becomes smaller and smaller. The model shows close agreement with two analytical approximations, namely the shallow ice approximation and Weertman thinning rate. Thermodynamic testing verified conduction, advection, and strain heating. Conduction dominated systems show temperature that varies linearly with depth. Systems that have advection show temperature inversions near the grounding line as cold surface temperatures are advected downstream. Strain heating shows as an increase in bed temperatures. The thermodynamic tests showed the temperature component computes temperatures correctly.

The application of the model to Whillans Ice Stream showed for constant softening in the slippery layer the velocity magnitude agrees with the measured velocity

magnitude fairly well. Linear downflow softening in the slippery layer gives velocities that are much larger than measured values. The interior ice shows plug flow dominates. Horizontal strain rate shows the extension in the ice with the largest values in the first 30 km of the flowline. Vertical strain rates complement horizontal strain rates for systems with or without the basal slippery layer. The Peclet number indicates regions of fast flow where advection dominates conduction. Calculated temperatures show advection dominated flow in agreement with large Peclet numbers and large velocities and conduction dominated flow where the Peclet number and velocities are small.

Future work includes implementing the use of the model as an embedded application in the map-plane University of Maine Ice Sheet Model (UMISM). Such an implementation allows the model to be linked with other existing model components in UMISM. The present model provides a good starting point for study of other ice streams. The present model provides convergence parameters to study the nonlinear nature of the problem from a chaos point of view. The present model could be improved with different computational strategies such as parallel programming, different meshing strategies that work toward minimizing aspect ratio, interactive graphics, and an interface for ease of use.

BIBLIOGRAPHY

- [1] West antarctic ice sheet stability and global sea level. <http://www.nsf.gov/pubs/1996/nstc96rp/sb4.htm>, 1996.
- [2] Ralph Baierlein. *Thermal Physics*. Cambridge University Press, New York, 1999.
- [3] J. L. Bamber, R. E. M. Riva, B. L. A. Vermeersen, and A. M. LeBrocq. Reassessment of the Potential Sea-Level Rise from a Collapse of the West Antarctic Ice Sheet. *Science*, 324:901–903, 2009.
- [4] E.B. Becker, G.F. Carey, and J.T. Oden. *Finite Elements, An Introduction*. Prentice-Hall, Englewood Cliffs, NJ, 1981.
- [5] S. F. Borg. *Matrix-Tensor Methods in Continuum Mechanics*. D. Van Nostrand Co., Inc., Princeton, 1963.
- [6] R. S. Brodkey and H. C. Hershey. *Transport Phenomena A Unified Approach*. McGraw-Hill, Inc., New York, 1988.
- [7] W.F. Budd, D. Jenssen, and U. Radok. Derived physical characteristics of the Antarctic Ice Sheet. Technical report, University of Melbourne Meteorology Dept. Publ. No. 18, Melbourne, Australia, 1971.
- [8] D. Dahl-Jensen. Steady thermomechanical flow along two-dimensional flow lines in large grounded ice sheets. *J. Geophys. Res.*, 94:10355–10362, 1989.
- [9] H.F. Davis and A.D. Snider. *Introduction to Vector Analysis*, Seventh Edition. Wm. C. Brown Publishers, Dubuque, IA, 1995.
- [10] J. Donea and A. Huerta. *Finite Element Methods for Flow Problems*. Wiley, New Jersey, 2003.
- [11] J.L. Fastook. The finite-element method for solving conservation equations in glaciology. *Computational Science and Engineering*, 1(1):55–67, 1993.
- [12] J.L. Fastook and A. Sargent. Better physics in embedded models. In *Eleventh Annual West Antarctic Ice Sheet Initiative Workshop*, Sterling, Virginia, 2004.
- [13] A.L. Fetter and J.D. Walecka. *Theoretical Mechanics of Particles and Continua*. McGraw-Hill, Inc., New York, New York, 1980.
- [14] Y.C. Fung. *A First Course in Continuum Mechanics*, Second Edition. Prentice-Hall, Inc., Englewood Cliffs, NJ, 1977.
- [15] J.W. Glen. The creep of polycrystalline ice. *Proceedings of the Royal Society of London*, 228:519–538, 1955.

- [16] P. M. Gresho, R. L. Sani, and M. S. Engelman. *Incompressible Flow and the Finite Element Method, Volume 2*. John Wiley & Sons, New York, 1998.
- [17] J. A. Griggs and J. L. Bamber. A New Thickness Dataset for the Antarctic Ice Shelves Derived From Satellite Altimetry. *in prep. Journal of Glaciology*, 2009.
- [18] R.LeB. Hooke. Flow law for polycrystalline ice in glaciers: Comparison of theoretical predictions, laboratory data, and field measurements. *Rev. Geophy. Space Phys.*, 19(4):664–672, 1981.
- [19] R.LeB. Hooke. *Principles of Glacier Mechanics*, Second Edition. Cambridge University Press, New York, 2005.
- [20] K. H. Huebner, D. L. Dewhirst, D. E. Smith, and T. G. Byrom. *The Finite Element Method for Engineers, Fourth Edition*. John Wiley & Sons, New York, 2001.
- [21] T. Hughes. *Ice Sheets*. Oxford University Press, New York, 1998.
- [22] Thomas J.R. Hughes. *The Finite Element Method: Linear Static and Dynamic Finite Element Analysis*. Prentice-Hall, Inc., New Jersey, 1987.
- [23] T.J. Hughes, G.H. Denton, B.E. Anderson, D. Schilling, J.L. Fastook, and C.S. Lingle. The last great ice sheets: A global view. In G. H. Denton and T. J. Hughes, editors, *The Last Great Ice Sheets*, pages 263–318. Wiley Interscience, New York, 1981.
- [24] P. Huybrechts. A 3-D model for the Antarctic Ice Sheet: A sensitivity study on the glacial-interglacial contrast. *Climate Dynamics*, 5:79–92, 1990.
- [25] L. D. Landau and E. M. Lifshitz. *Fluid Mechanics*. Pergamon, London, 1959.
- [26] H. Leipholz. *Theory of elasticity*. Noordhoff International Publishing, Leyden, The Netherlands, 1974.
- [27] D.R. MacAyeal. Large-scale ice flow over a viscous basal sediment: Theory and application to Ice Stream B, Antarctica. *Journal of Geophysical Research*, 94(B4):4071–4087, 1989.
- [28] D.R. MacAyeal. *EISMINT: Lessons in Ice-Sheet Modeling*. University of Chicago, Chicago, Illinois, 1997.
- [29] C. Fox Maule, M. E. Purucker, N. Olsen, and K. Mosegaard. Heat Flux Anomalies in Antarctica Revealed by Satellite Magnetic Data. *Science*, 309(DOI: 10.1126/science.1106888):464, 2005.
- [30] W. D. Means. *Stress and Strain*. Springer-Verlag, New York, 1976.

- [31] G. V. Middleton and P. R. Wilcock. *Mechanics in the Earth and Environmental Sciences*. Cambridge University Press, New York, 1994.
- [32] L.W. Morland. Unconfined ice-shelf flow. In C.J. van der Veen and J. Oerlemans, editors, *Dynamics of the West Antarctic Ice Sheet*. D. Reidel, Boston, 1987.
- [33] F. O. Nitsche, S. S. Jacobs, R. D. Larter, and K. Gohl. Bathymetry of the Amundsen Sea Continental Shelf: Implications for Geology, Oceanography, and Glaciology. *Geochemistry, Geophysics, Geosystems*, 8(doi:10.1029/2007GC001694):Q10009, 2007.
- [34] J.F. Nye. The mechanics of glacier flow. *Journal of Glaciology*, 2(12):82–93, 1952.
- [35] F. K. G. Odqvist. *Mathematical Theory of Creep and Creep Rupture*. Oxford University Press, London, 1974.
- [36] R. L. Panton. *Incompressible Flow*. Wiley-Interscience, New York, 1984.
- [37] T. C. Papanastasiou, G. C. Georgiou, and A. N. Alexandrou. *Viscous Fluid Flow*. CRC Press, Boca Raton, 2000.
- [38] S. V. Patankar. *Numerical Heat Transfer and Fluid Flow*. McGraw-Hill, Inc., New York, 1980.
- [39] W.S.B Paterson. *The Physics of Glaciers*, Third Edition. Elsevier Science Ltd., Oxford, 1994.
- [40] A. J. Payne, P. Huybrechts, A. Abe-Ouchi, R. Calov, J. L. Fastook, R. Greve, S. J. Marshall, I. Marsiat, C. Ritz, and L. Tarasov. Results from the eismint phase 2 simplified geometry experiments: The effects of thermomechanical coupling. *Journal of Glaciology*, 46(153):227–238, 2000.
- [41] J. N. Reddy. *An Introduction to Nonlinear Finite Element Analysis*. Oxford University Press, New York, 2004.
- [42] G.de Q. Robin. Ice movement and temperature distribution in glaciers and ice sheets. *Journal of Glaciology*, 2:523–532, 1955.
- [43] D. G. Vaughan, J. L .Bamber, M. Giovinetto, and A. P. R. Cooper. Reassessment of Net Surface Mass Balance in Antarctica. *Journal of Climate*, 12:933–946, 1999.
- [44] J. Weertman. Deformation of floating ice shelves. *Journal of Glaciology*, 3:38–42, 1957.

BIOGRAPHY OF THE AUTHOR

Debra Ann Kenneway was born in Portland, Maine on April 22, 1967. She graduated from South Portland High School in 1985. Debra attended the University of Maine for three years as a psychology major and in 1987 she broke the discus record in outdoor track set previously in 1978 by Anne Turbyne. From 1988 to 1992, she worked as a licensed veterinary technician, after passing the exam given by the State of Maine Board of Veterinarians. In June of 1988 she married Bruce Kenneway. Her daughter Regina was born in the fall of 1989, and her daughter Charlotte was born in the fall of 1991.

Debra worked at Digital Link in Sunnyvale, CA from 1994 to 1995. She maintained the company database and generated financial reports. She left Digital Link to attend San Jose State University. She double majored in Physics and Mathematics. While at San Jose State University she was the recipient of the Barnum-Everett scholarship, she was awarded an NSF award, Grant Number 21-1507-1723, for the Research Experience for Undergraduates program, she was elected to the Golden Key National Honor Society, and she received the Deans Scholar Award. Debra researched frustration in condensed matter and she also independently researched methods of solution of ordinary differential equations.

From 1997 to 2000 Debra worked for Peoples Heritage Financial Group. She maintained a database for the commercial division, provided network support and user support, and wrote code to automate processes. Her son John was born in the summer of 1998. While working full time, she attended the University of Southern Maine for the next two years as a mathematics major. In 2000 she received her Bachelor of Arts in Mathematics from the University of Southern Maine, graduating summa cum laude. Debra was accepted as a graduate student at the University of

Maine in the Department of Physics and Astronomy in 2000. While there, she was a teaching assistant, a research assistant, and received Federal Work Study. Debra received a Maine Economic Improvement Fund Summer Graduate Research award in 2004. Debra received her Master of Science in Physics in 2005.

From 2007 to 2009 Debra taught 9th grade science and biology at Old Town High School. She has been an active member of her community coaching a season of farm league baseball in 2007 and assistant coaching ice hockey for ages 11 and younger from 2006 to 2008. Debra plays recreational hockey and is the goalie for her team. She received her blue belt in ATA Tae Kwon Do in 2010. Debra received the Frank Todd scholarship from the Department of Physics and Astronomy twice. Debra is a candidate for the Doctor of Philosophy degree in Physics from the University of Maine in May, 2010.